Chapter 2

Thermal Ignition of Gaseous Fuel-Air Mixtures Within a Slowly Heated Vessel [1]

2.1 Introduction

As discussed in Chapter 1, a better understanding of thermal ignition, specifically auto-ignition, is important for safety regulations and engineering design. While a standard test for the auto-ignition temperature, the ASTM (2005), exists, only the minimum temperature for ignition at atmospheric pressure is investigated for a given geometry and size. Additionally, the specific mixture composition is neither controlled nor measured as the liquid test fuel is injected into a heated open vessel. The contents are not actively mixed and it is presumed that a considerable range of composition exists within pockets of gas in the vessel as evaporation of liquid fuel occurs (Pilling, 1997).

Our approach in this study was to precisely control the composition of the gas mixture allowing for comparison with numerical models, while monitoring the temperature and pressure as well as the fuel concentration. Through accurate control of the heating rate, its effect on the combustion can also be studied. Hexane was selected as a test fuel. It has a similar auto-ignition temperature of 498 K (Kuchta et al., 1965, Kuchta, 1985) to kerosene and is comparable to jet fuel or turbine fuel (CRC, 1983, Colwell and Reza, 2005) at 511 K. Additionally, Hexane is easy to handle in liquid form but vaporizes readily, and detailed chemical reaction mechanisms are available.

An extension of the classical Semenov theory (Semenov, 1940), described later in this chapter, can be used to model the auto-ignition process in a closed vessel that is slowly heated from ambient

[1] The work in this chapter has been published in large part in Boettcher, P. A., Mével, R., Thomas, V. and Shepherd, J. E. The effect of heating rates on low temperature hexane air combustion. *Fuel* (2012), doi:10.1016/j.fuel.2011.12.044

conditions. This model of the reactor can be used with either a detailed chemical mechanism that fully represents the complex chemistry of n-hexane or with a one-step model that is more easily understood analytically. Both approaches are presented in this chapter. The experimental and computational results are compared and a detailed analysis is given of the role of heat transfer and reactant consumption on the progress of the explosion.

2.2 Experiments

2.2.1 Experimental Setup

The test vessel (Figure 2.1) is a closed 400 mL Pyrex cell (surface to volume ratio ≈ 0.85 cm^{-1}). Prior to each experiment, the test cell is evacuated to less than 10 Pa. The vessel is then filled with n-hexane, nitrogen, and oxygen using the partial pressure method, then thoroughly mixed by a circulation pump. Hexane is injected as a liquid through a septum at a partial pressure below its vapor pressure. This ensures complete vaporization. The uncertainty in composition is due to the accuracy $\pm$ 0.01 kPa of the pressure measurement. Two sapphire windows are spaced 9 cm apart, providing optical access for the laser measurement. The vessel is suspended inside an aluminum shell with an air gap of approximately 3 mm, and the shell is heated by two band heaters rated at a total of 800 W. The temperature inside the vessel is measured by a K-type thermocouple that has been coated with silica in order to avoid catalytic effects. During the experiment, transient pressure is measured with a separate fast-response static pressure gage ($\geq$ 10 kHz). The final heating rate is computed from the pressure measurements using the values before the onset of the reaction. Assuming no change in moles, using the ideal gas law, the heating rate can be computed from the pressure trace using

$$\frac{dT}{dt} = \frac{V}{n\tilde{R}}\frac{dP}{dt} \, . \tag{2.1}$$

This method is preferred over measurements using thermocouples because the response time of the pressure transducer is much shorter than that of the thermocouple. The data is directly analyzed and averaged giving an effective sampling rate of 8 Hz. When a specified drop in fuel concentration is detected, a second data acquisition board is triggered that stores data at 150 kHz during a rapid ignition event.

Experiments were performed at three total pressures: 26, 67, and 101 kPa, three equivalence ratios, ϕ: 0.6, 1, and 1.2, and heating rates between 4 K/min and 14 K/min.

The fuel concentration is measured by direct absorption (Klingbeil et al., 2006, Drallmeier, 2003).

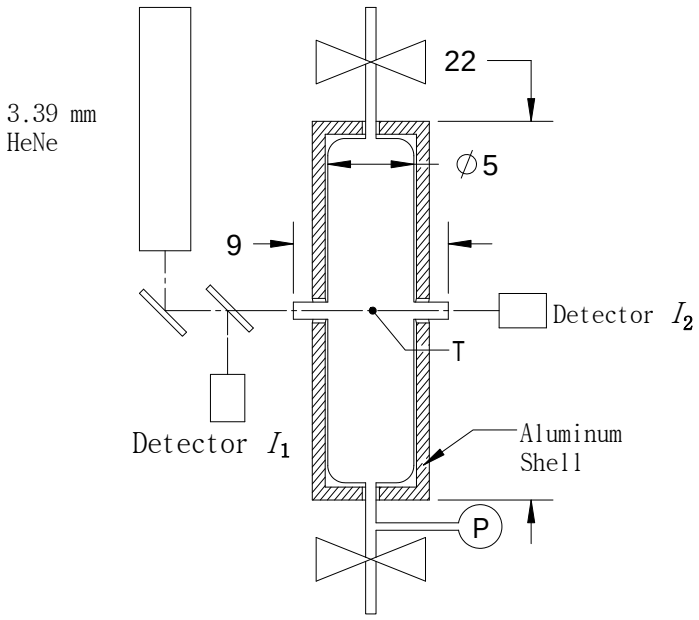

Figure 2.1: Schematic of the experimental setup (all dimensions are in cm)

A commercially available 3.39 μm HeNe laser is passed through a chopper running at 300 Hz. The beam is split two ways before entering the test cell through a 0.5 mm thin sapphire window. The main beam passes through the test cell and is measured by a detector on the other side, while the second beam is sent to a reference detector to correct for variations in the initial laser intensity. High angles of incidence ($\sim 10°$) were used to avoid intensity changes due to interference effects from the windows caused by thermal expansion since internal reflections are scattered through a wider angle.

The n-hexane mole fraction is calculated from the detected laser transmission using Beer's law. The C-H bond in any hydrocarbon molecule absorbs at the 3.39 μm wavelength; changes from n-hexane into other hydrocarbon molecules other than C_1 species cannot be detected Mével et al. (2012). Thus, an equivalent n-hexane mole fraction, $X^*_{C_6H_{14}}$, is calculated based on the absorption cross section of n-hexane, which is found through separate calibration experiments to be $\sigma_\nu = 38 \pm 1$ m^2/mole. This value is in agreement with values from the literature (Jaynes and Beam found 45 m^2/mole (Jaynes and Beam, 1969), Drallmeier 38.5 $\pm$ 2 m^2/mole (Drallmeier, 2003, Klingbeil et al., 2006), Tsuboi et al. 36.2 $\pm$ 7 m^2/mole (Tsuboi et al., 1985, Klingbeil et al., 2006)). Further measurements have been performed by Mével et al. (2012) that show that the absorption cross section is constant for hexane from 303–413 K and the value can thus be assumed to be constant. The intensity changes are related to the equivalent partial pressure of fuel, P^*_{fuel}, via Beer's Law,

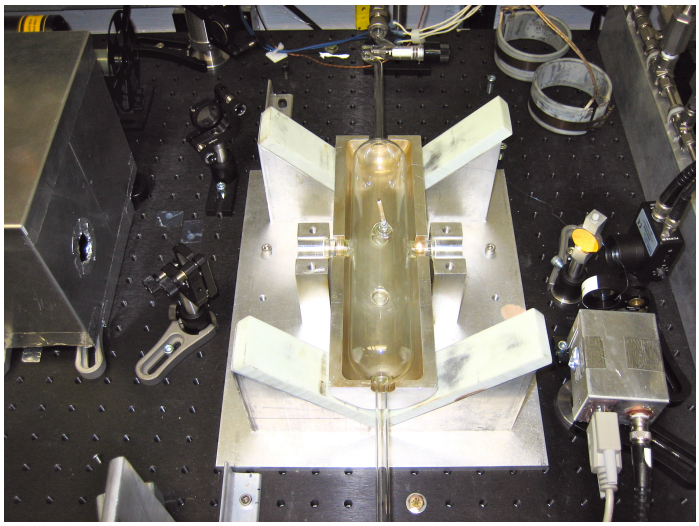

Figure 2.2: Pictures of the heated experimental vessel setup

$$\frac{I}{I_0} = \exp\left(-\frac{\sigma_\nu P^*_{fuel} L}{\tilde{R}T}\right) , \tag{2.2}$$

where I is the laser intensity signal, I_0 is the signal intensity without any absorbing species present, σ_ν is the absorption cross section, L is the path length, $\tilde{R}$ is the universal gas constant, and T is the temperature.

As described above only an equivalent partial pressure of fuel or equivalent hexane mole fraction can be measured with this technique. The final equivalent mole fraction of n-hexane is given by

$$X^*_{C_6H_{14}} = \frac{P^*_{fuel}}{P_{total}} = \frac{\tilde{R}T}{\sigma_\nu L P_{total}} \left[\ln\left(\frac{I_1(t)}{I_2(t)}\right) - \ln\left(\frac{I^0_1}{I^0_2}\right)\right] , \tag{2.3}$$

where I_1 is the reference detector, and I_2 is the signal detector on the other side of the absorption path, and the superscript 0 represent their values before fuel is added. Additional details are given in Appendix A.

2.2.2 Experimental Results

Experiments were performed varying the composition, initial pressure, and heating rate applied to the vessel walls. Figures 2.3 and 2.4 show the temperature, pressure, and fuel mole fraction during two representative experiments performed with a slightly fuel-rich mixture ($\phi = 1.2$, 2.6 % n-hexane in air) and at a initial pressure of 101 kPa. The mixture of Fig. 2.3 was heated at a rate of 4.25 K/min and underwent a slow reaction. A slow reaction case is characterized by a slow consumption of the

fuel with a minimal pressure rise. The mixture of Fig. 2.4 was heated at 11 K/min and underwent ignition. In this context, an event characterized by rapid consumption of the fuel accompanied by a large pressure rise will be referred to as either an ignition case or fast reaction case.

The slow reaction case (Fig. 2.3) has several features that make it significantly different from the ignition case. As the temperature increases from room temperature, we observe a slow consumption of the fuel (reduction in concentration of C-H bonds) starting at 500 K (2500 s), which reduces the fuel concentration from 2.6% to 0.45% over 250 s until the heating system is turned off at 540 K. During this time neither the pressure nor the temperature rise significantly above the trajectory prescribed by the input heating rate.

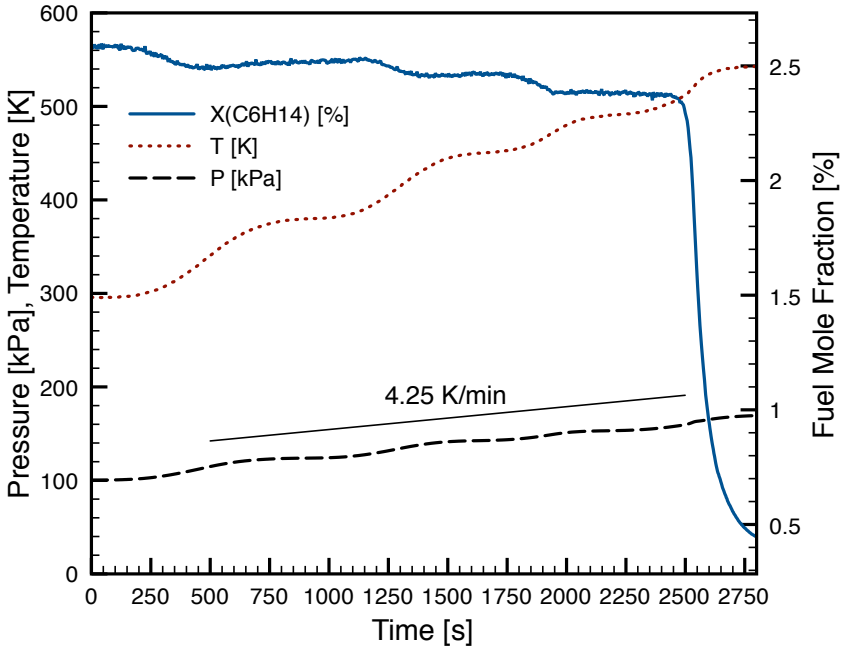

Figure 2.3: Slow reaction of a fuel-rich ($\phi = 1.2$) n-hexane/air mixture at an initial pressure of 101 kPa heated at 4.25 K per minute (note that the heating rate is computed from the pressure signal)

The temperature and pressure plot show small steps in the ramp from room temperature to 540 K. These steps are due to the response time of the controller and the aluminum shell to the overall heating rate and temperature change during the initial fuel consumption is 4.25 K/min.

Heating the same mixture ($\phi = 1.2$) at roughly twice the heating rate, 11 K/min, results in a fast reaction (Fig. 2.4). Upon ignition, we observe a spike in pressure, reaching a peak of 330 kPa with elevated pressure for 0.5 seconds. The temperature peak is visible but substantially smaller due to the much slower response time of the thermocouple as compared to the pressure transducer.

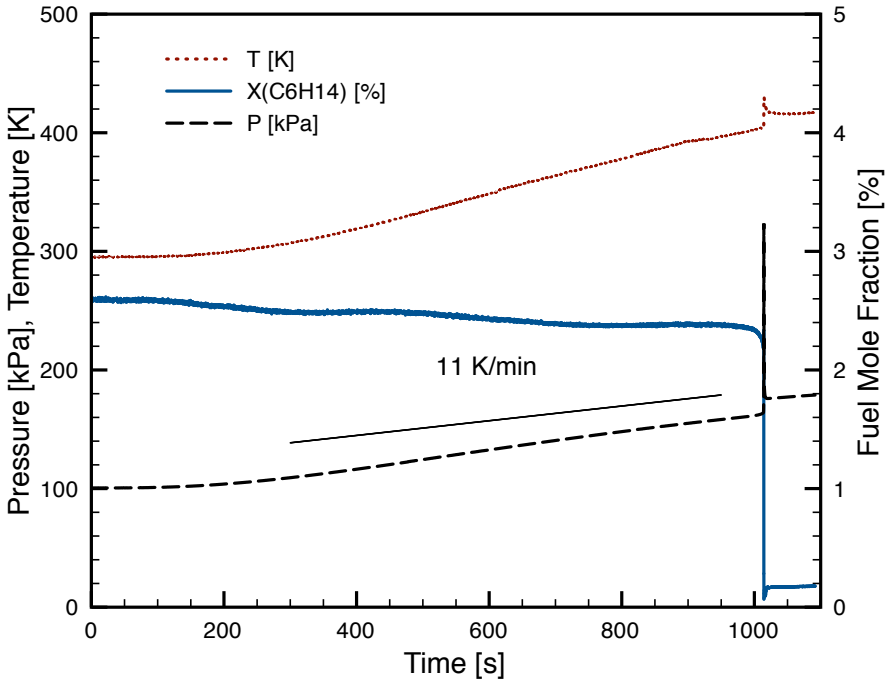

Figure 2.4: Ignition of a fuel-rich ($\phi = 1.2$) n-hexane/air mixture at an initial pressure of 101 kPa heated at 11 K per minute (note that the heating rate is computed from the pressure signal)

From the changes in the fuel concentration, temperature, and pressure measurements, we observe that the fast reaction occurs at 1010 s. At this time, we estimate the temperature in the vessel to be 473 K (200 °C), whereas the thermocouple reads 400 K. Due to the limited response rate of the thermocouple, discussed earlier, the actual gas temperature must be inferred from the pressure measurements, using the assumption that the mixture is an ideal gas and negligible changes in the number of moles. At 1000 s we see an initial decrease in fuel concentration followed by a rapid consumption of the fuel during the ignition transient at $\sim$ 1010 s. Unlike the slow reaction, in this case, the response of the measurement system is limited by signal contamination from light emission during the ignition.

The effect of initial pressure and composition was examined for 14 conditions and the outcomes are shown in Figure 2.5. The following changes in the experimental conditions transition the system from a slow reaction to an ignition: (1) increasing the pressure (26–100 kPa), (2) increasing the heating rate (4–12 K/min), (3) increasing the equivalence ratio in the region investigated ($\phi = 0.6 - -1.25$). Each of these factors is confirmed experimentally, while keeping the other two parameters constant.

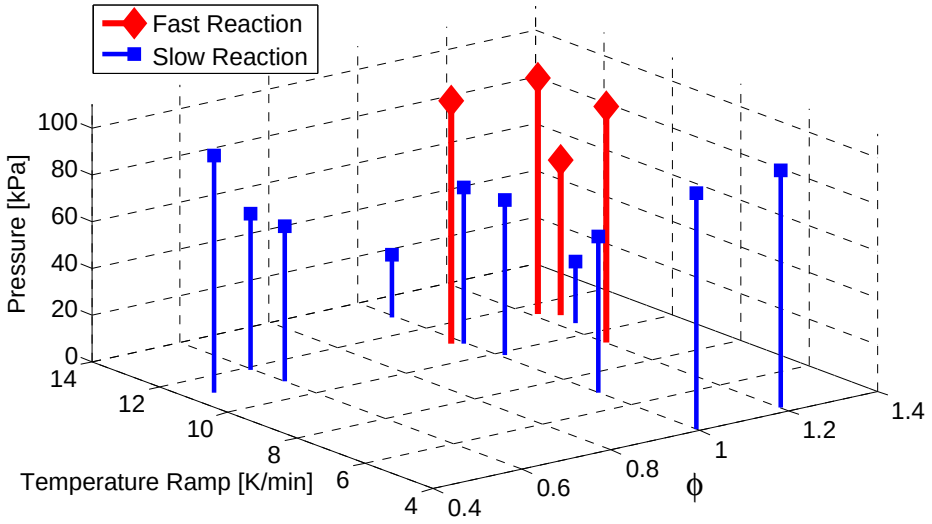

Figure 2.5: Experimental results as a function of total pressure, temperature ramp rate, and equivalence ratio

2.2.3 Simultaneous Measurements of Oxygen and Fuel [2]

In addition to the fuel concentration measurements, an attempt has been made to spectroscopically monitor the molecular oxygen concentration during the heating rate experiments. Since transitions in the A band near 760 nm are spin forbidden, direct absorption measurements of O_2 are complicated by the very weak absorption cross sections (Philippe and Hanson, 1993). One method for overcoming this limitation is the use of a derivative technique of spectroscopy with second harmonic (2f) detection as demonstrated by Kroll et al. (1987), Philippe and Hanson (1993), and Rieker et al. (2009). This technique consists of modulating, at a high frequency, the output wavelength of the laser diode, by modulating the diode's current input, allowing a fast scanning across the absorption line. Assuming a perfect gas the second derivative of the signal intensity can be linked to the oxygen partial pressure by the following:

$$\left.\frac{d^2 I}{d\nu^2}\right|_{\nu=\nu_0=\tilde{\nu}} = c_0 + c_1 P_{O_2} \tag{2.4}$$

where σ_ν is the absorption cross section, c_0 and c_1 are constants obtained through a calibration procedure. Further details are given in Appendix B.

[2]The author would like to thank Raza Akbar, Greg Rieker, Adrianus Indrat Aria, Bryan Hires, and David Gutschick for their help with the 2f detection.

2.2.3.1 Experimental Setup and Calibration Procedure

The experimental arrangement is shown in Figure 2.6 [3]. It consists of a signal generator, a summing amplifier, a laser diode with current and temperature controllers, a lock-in amplifier, a low noise preamplifier with bandpass filter, and a waveform recorder. The signal generator is used to create a sawtooth-like carrier signal with a frequency of 80 Hz and an amplitude of $\sim$ 100 mA. This signal scans across the absorption line. The second signal, the sine wave, is generated by the lock-in amplifier's internal signal generator with a frequency of 23.5 kHz and an amplitude of 4 mA. These signals are summed and then sent to the laser diode current controller. Both the sine wave signal and the transmitted laser diode beam are collected by the lock-in detector. The resulting signal is then filtered and recorded by the waveform recorder.

The height of the 2f peak is calibrated against the partial pressure of oxygen. Figure 2.7 shows that the peak height varies linearly with the amount of oxygen as predicted from Equation 2.4 for the range of oxygen concentrations investigated. For calibration, the vessel is first evacuated to below 10 Pa and then filled with increasing amounts of oxygen. The second calibration was performed by first filling the vessel 67 kPa of N_2 and then mixing the oxygen with the nitrogen in increasing steps. The linear constant is reduced when nitrogen is added, which is expected due to the effect of pressure broadening. Also indicated in Figure 2.7 is the uncertainty in the calibration measurement. This uncertainty is strictly based on the evaluation of the standard deviation of the time series data acquired over the measurement interval, typically 30 seconds. The uncertainty in the pressure is less than the indicated symbol size. The calibration was performed at room temperature.

2.2.3.2 Application of Oxygen Measurements

The measurement of oxygen concentration was only implemented successfully once during the course of this investigation. The experimental technique has proven to be extremely sensitive to the variations in the optical path. The experimental procedure of heating the vessel from room temperature to the auto-ignition temperature causes the glass vessel to expand substantially. This produces both an etalon effect and beam steering, which we were only able to correct for by using a nonreactive mixture for one data set. Figure 2.8 shows the consumption of the oxygen and fuel for a fuel-rich mixture ($\phi = 1.2$) at a low initial pressure ($P_0 = 26.67$ kPa) heated at a 11.2 K/min. The measurements show consumption of the fuel and oxygen at the same time, which agrees with the simulation results of the slow reaction shown in Figure 2.12 (a). This result agrees with the overall trends shown

[3] This figure was adapted from a figure created by Adrianus Indrat Aria, Bryan Hires, and David Gutschick.

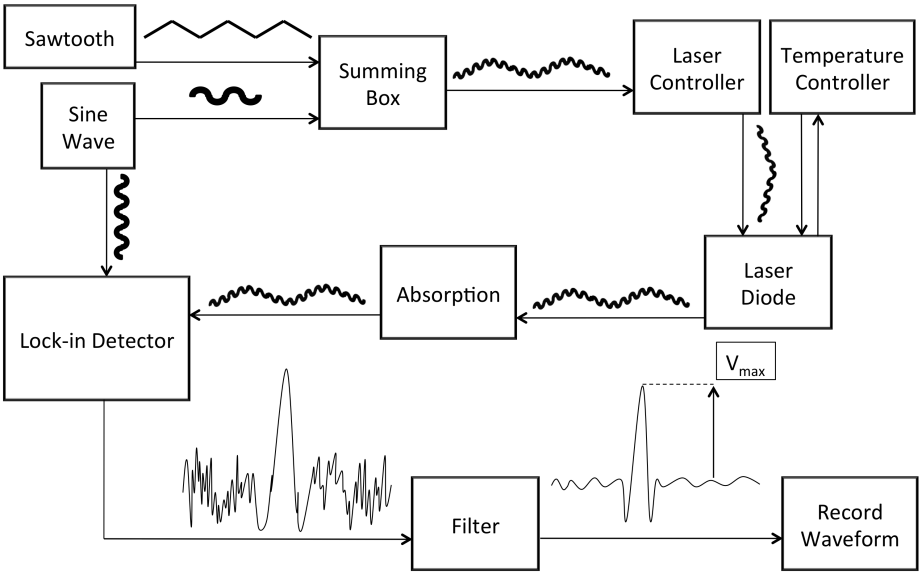

Figure 2.6: Schematic of the experimental setup for molecular oxygen measurements

in Figure 2.5, which show that reducing pressure, heating rate, or equivalence ratio sufficiently in the range investigated leads to a slow reaction of the mixture instead of ignition.

For future experiments, the limitations shown here could be addressed in several ways. First, the impact of the optical path variations could be reduced by increasing the test cell dimension or isolating the windows mechanically from the test cell. Additionally, the sensitivity of the measurements could be increased by evacuating or nitrogen flushing the laser beam path outside the test cell, avoiding perturbations due the oxygen contained in air. Finally, the overall experimental procedure could be adapted to start the temperature ramp at a higher temperature, reducing the total temperature change.

2.3 Modeling

2.3.1 Modeling with a Detailed Chemical Mechanism

The experiment is modeled using Semenov's theory (Semenov, 1940) for thermal ignition, assuming a well stirred constant volume reactor filled with a uniform mixture of n-hexane in air. The wall temperature is increased from room temperature at a constant rate, α, which is included in the energy equation as: $T_w = T_w^0 + \alpha\, t$. The temperature variation with time is computed from the

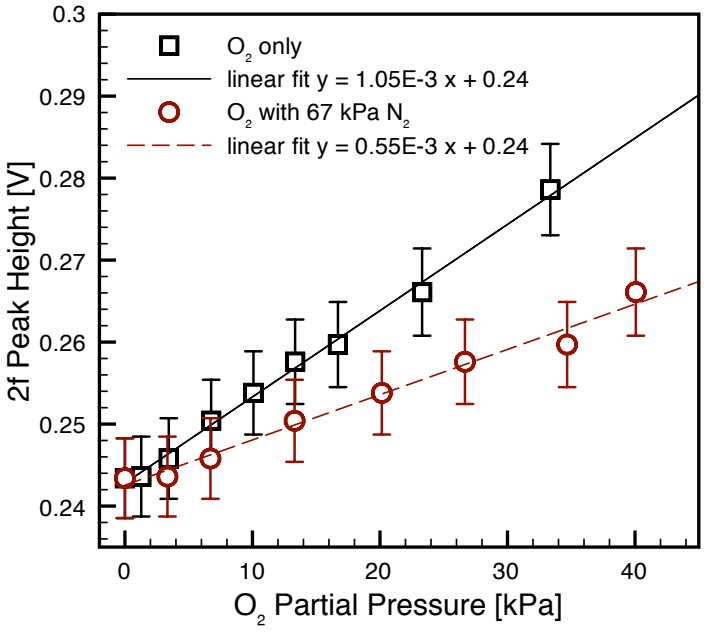

Figure 2.7: Calibration curve, second harmonic peak height as a function of molecular oxygen partial pressure with $\pm\,\sigma$ uncertainty bars (O_2 only and O_2 with 67 kPa N_2 dilution)

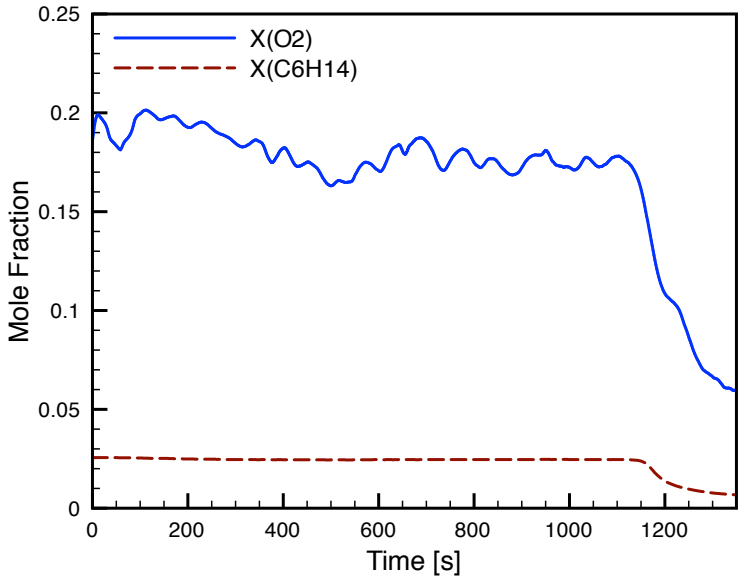

Figure 2.8: Measurement of the molecular oxygen and fuel concentration during a slow reaction for a n-hexane/air mixture. Conditions: $P_0 = 26.67$ kPa, $\phi = 1.2$, $\alpha = 11.2$ K/min

energy conservation equation for a well-stirred closed volume:

$$V\rho c_v \frac{dT}{dt} = V\sum_{i=1}^{k} \dot{\omega}_i u_i + Sh\left(T_w^0 + \alpha\, t - T\right) = \dot{q}_r + \dot{q}_w. \tag{2.5}$$

The species variation with time is computed with the mass conservation equation for a closed volume

$$\frac{dY_i}{dt} = \frac{W_i \dot{\omega}_i}{\rho} \qquad i = 1, 2, \ldots, k \tag{2.6}$$

where k is the total number of species. The vessel volume, V, and surface area, S, are constant while the density, ρ, and specific heat at constant volume, c_v, are calculated at each solver time step. The heat transfer is modeled with Newton's law of cooling using a lumped parameter, h, to approximate free convection inside the vessel. The change in temperature is determined by the competition between the chemical heat release, $\dot{q}_r$, and the heat-loss rate, $\dot{q}_w$, into which the terms of the energy equation have been grouped. Cantera (Goodwin, 2003) is used to compute the net chemical production rate, $\dot{\omega}_i$, utilizing a detailed chemistry mechanism, as well as all thermodynamic properties for both individual species and the gas mixture as a whole. A variable-coefficient ODE solver (VODE) is used to integrate the system of equations (Brown et al., 1989).

The basis for our reaction mechanism is the detailed model of Ramirez et al. (2011). This kinetic scheme was developed to model decane and biofuel chemistry. Further validation for n-hexane was necessary for the present study; this is presented along with the modeling results. The mixture is initialized at a given pressure, temperature, and equivalence ratio, and then the energy equation is integrated forward in time with the wall temperature rising at a specified rate, α.

In order to model this system, a detailed kinetic scheme had to be identified and validated against appropriate low temperature data. Although hydrocarbons have been widely studied, there exists little data concerning n-hexane oxidation (Simmie, 2003). Curran et al. (1995) studied hexane isomer chemistry through the modeling and measurement of exhaust gases from an engine. Shock tube experiments have been performed by Burcat et al. (1996) and Zhukov et al. (2004). Kelley et al. (2011) recently reported laminar flame speeds for C-5 to C-8 n-alkanes. To our knowledge, no low temperature experimental data exists for n-hexane-oxygen mixtures. It should also be noted that no single detailed kinetic scheme is available to model n-hexane combustion chemistry from low to high temperature. In order to describe the kinetics of n-hexane-air mixtures, we employed the C-7 basis of the detailed model published by Ramirez et al. (2011) which includes n-hexane.

2.3.1.1 Kinetic Scheme Validation

For validation at high temperature, we used the experimental data of Burcat et al. (1996) and Zhukov et al. (2004). For validation at intermediate and low temperature, we used n-heptane flow reactor and jet stirred reactor data from Held et al. (1997) and Dagaut et al. (1995), respectively.

The experimental *n*-hexane-oxygen-diluent mixture auto-ignition delay times from (Burcat et al., 1996) and (Zhukov et al., 2004) are compared in Fig. 2.9 to the predictions of the Ramirez model. The computed delay times are in reasonable agreement with the experimental results. Although the model typically underestimates the results of Burcat in the high-temperature range, the mean relative error does not exceed 30%. The mean error with respect to the data of Zhukov is around 25%. Considering the usual uncertainty of 20% associated with shock-tube delay times, the model reproduces the experimental data adequately for the purpose of the present study.

The flow reactor experimental data from Held et al. (1997) are compared in Fig. 2.10 (a) to the model predictions for a lean n-heptane-oxygen-nitrogen mixture. The temporal mole fraction profiles of the main species are relatively well predicted. The consumption of both reactants, C_7H_{16} and O_2, are satisfactorily predicted throughout the experiment, whereas the production of CH_4 and C_2H_4 are overestimated early in the oxidation process, and CO mole fraction is underestimated. It should also be noted that the temperature profiles (not shown) are in good agreement with experiments.

The jet-stirred reactor experimental data from Dagaut et al. and the model predictions are compared in Fig. 2.10 (b) for a stoichiometric n-heptane-oxygen-nitrogen mixture. The CO mole fraction is well predicted everywhere except within the negative temperature coefficient region (NTC), where an increase in temperature leads to longer induction times (700–800 K). Figure 2.10 (b) shows that the CO_2 mole fraction is underestimated in the low temperature range, but is in close agreement in the high-temperature range. The CH_4 mole fraction is overestimated throughout most of the temperature range. Finally, it can be noted that the NTC region position is correctly predicted.

The last experimental datum to be modeled in testing the validity of the detailed kinetic scheme is the auto-ignition temperature. The experimental value is near 500 K for a stoichiometric *n*-hexane-air mixture at atmospheric pressure. The predicted temperature, based on a constant-volume reactor simulation, is 540 K.

Although the model is not able to reproduce the whole set of selected experimental data with good accuracy, the general trends of *n*-hexane-oxygen mixture reactivity are predicted. A better agreement might be obtained by adjusting the dominant kinetic parameters. However, this would require additional experimental data and is beyond the scope of the present study.

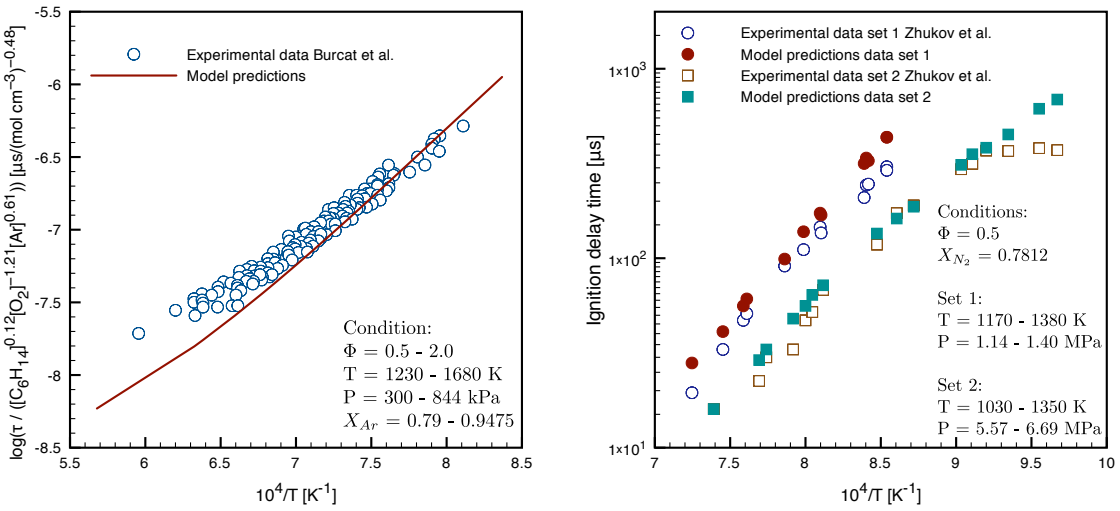

(a) (b)

Figure 2.9: Comparison of shock tube experimental data to the predictions of the Ramirez model for *n*-hexane-oxygen-argon mixture. (a) data of Burcat et al. (1996) (b) data of Zhukov et al. (2004)

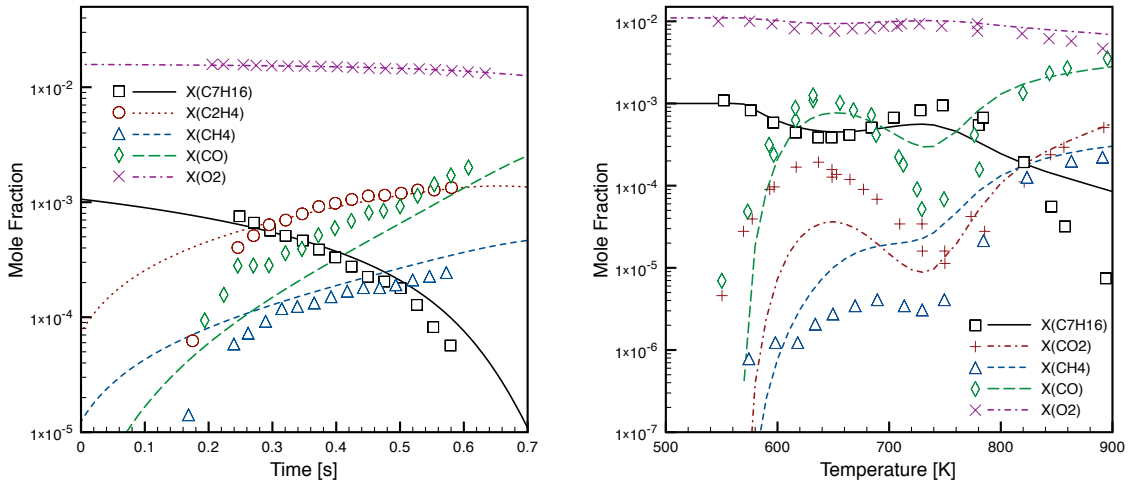

(a) (b)

Figure 2.10: Comparison of flow and jet-stirred reactor experimental data to the predictions of the Ramirez model for n-heptane-oxygen-nitrogen mixtures. (a) flow reactor data from Held et al. (1997). Conditions: $\phi = 0.79$; $T = 930$ K; $P = 303$ kPa; $X_{N2} = 0.9831$. (b) jet-stirred reactor data from Dagaut et al. (1995), Conditions: $\phi = 1$; Residence time = 1 s; $P = 1010$ kPa; $X_{N2} = 0.988$

2.3.1.2 Fast and Slow Combustion Modeling

The purpose of the modeling study was to determine if an existing reaction mechanism could qualitatively reproduce the observed trends using a simple reactor model that simulates the key features of the present experimental setup. The reactor was modeled as a homogenous mixture in a closed, fixed volume with a specified, time-varying wall temperature. Heat transfer from the vessel wall to the contents is characterized through the wall heat transfer coefficient, h, with a value of 15 W/m^2-K. The value of the heat transfer coefficient was determined iteratively until the switch between the slow and fast reaction was observed for heating rates of 5 and 10 K/min and is consistent with heat transfer from free convection of gases (White, 1984).

Figures 2.11–2.12 present the simulation results for a slow reaction and an ignition event corresponding to a rich mixture, $\phi = 1.2$, with heating rates of 5 and 10 K/min, respectively. In the case of the slow reaction, a slight increase in temperature and pressure can be seen around 2900 s. This time corresponds to the maximum rate of n-hexane and oxygen consumption. Reactant consumption extends over a long period of time, several hundred seconds. Although the mixture is rich, only 75% of the oxygen is consumed after 3100 s. In the case of the ignition event, a sharp increase in temperature and pressure is observed at about 1500 s. At this time, reactants are consumed and products are formed over a short period of time, on the order of tens of milliseconds. Figures 2.11 and 2.12 demonstrate that reactant consumption proceeds at essentially constant temperature and pressure in the case of a slow reaction event, and tends towards a constant volume explosion in the case of a fast combustion event.

It is remarkable that a variation of a factor of two in the heating rate results in a completely different mode of combustion in these two cases. Further the temperature at which strong reactant consumption occurs is actually lower in the higher heating rate case (473 K) than in the lower heating case (500 K).

2.3.1.3 Heat Production and Losses

In order to help understand the differences between the slow reaction and ignition cases, the heat production and loss rates have been calculated, along with the energy release rate for each elementary reaction (Figures 2.13 and 2.14).

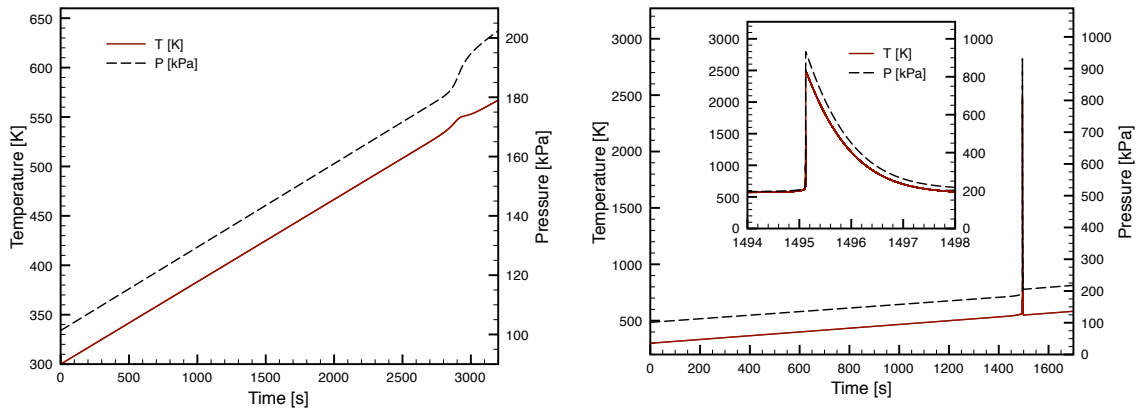

Figure 2.11: Simulated temperature and pressure profiles for a n-hexane-air mixture for two different heating rates. Conditions: $\phi = 1.2$ (a) $\alpha = 5$ K/min (b) $\alpha = 10$ K/min

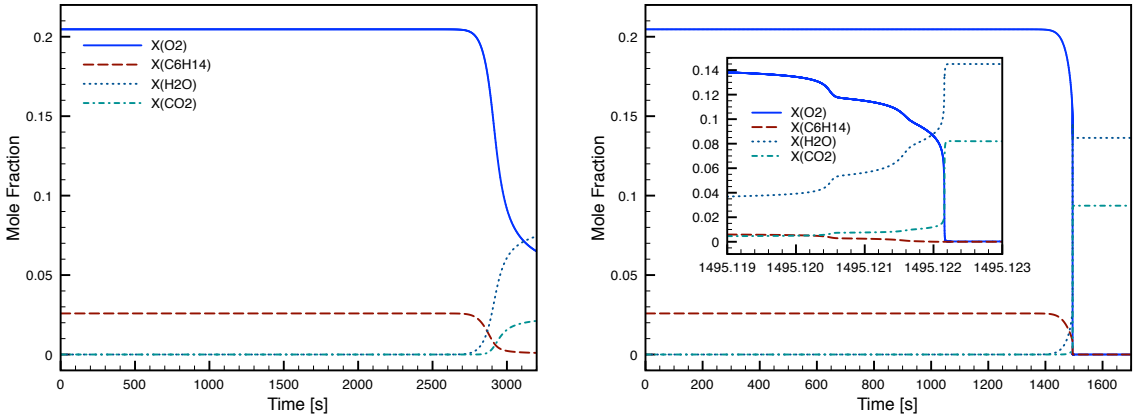

Figure 2.12: Simulated species profiles for a n-hexane-air mixture for two different heating rates. Conditions: $\phi = 1.2$ (a) $\alpha = 5$ K/min (b) $\alpha = 10$ K/min

The heat release term, $\dot{q}_r$, and the magnitude of the heat-loss term, $|\dot{q}_w|$, from Equation 2.5, are shown in Figure 2.13 (note that the time axes are scaled so that temperature history will coincide in the absence of chemical reactions). The initial value of the heat-loss term corresponds directly to the heating rate to the reactor. The inset shows the slight lag of the heat-loss term in comparison to the heat release term. For the slow reaction case, the difference diminishes as the reaction becomes less exothermic, while for the ignition case the difference increases as mixture move towards the ignition point. In the slow reaction case, the chemical heat release is balanced by heat-loss at the wall. In the ignition case, the energy release exceeds the heat-loss at the wall by several orders of magnitude when ignition occurs. The energy release by the chemical reactions is $\sim 10^7$ times greater during an ignition case than during the slow reaction case. The difference in chemical reaction pathways is

shown by the fact that the slow reaction heat release peaks before the ignition case does.

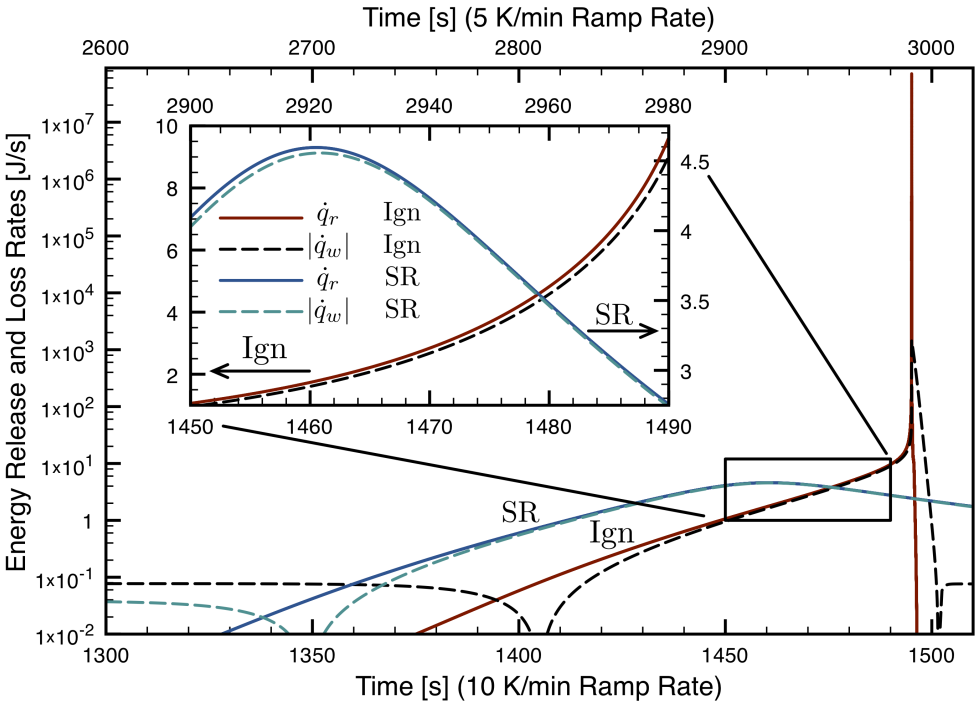

Figure 2.13: Chemical heat production and heat-loss rates for a n-hexane-air mixture for two different heating rates. Conditions: $\Phi = 1.2$; $\alpha = 5$ K/min and $\alpha = 10$ K/min (Ignition — Ign, Slow Reaction — SR)

The chemical reactions producing and consuming heat are very different (Fig. 2.14) for the slow and fast reaction cases. In the slow reaction case, the reactions that release energy involve weakly reactive species such as HO_2, H_2O_2, and alkylperoxides. Although most of these reactions are highly exothermic, they proceed at a slow rate, keeping the energy release rate low. In the ignition case, the energy release is driven by two reactions: H + OH + M $\Longleftrightarrow$ H_2O + M and CO + OH $\Longleftrightarrow$ CO_2 + H. These reactions produce the two main reaction products, H_2O and CO_2, and are very exothermic.

2.3.1.4 Radicals and Atoms Rate of Production

The previous analyses demonstrates that the heating rate of the reactor controls the thermodynamic conditions which in turn control the chemical pathways. The dominant chemical pathways for each case are analyzed via detailed species rate of production and reaction pathway diagrams.

Rate of production analysis have been performed for O and H atoms, as well as, OH and HO_2

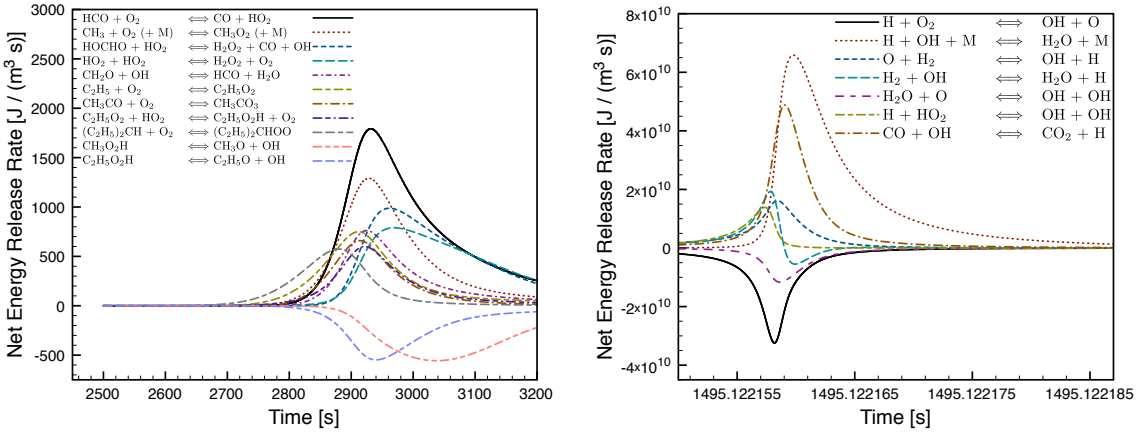

(a) (b)

Figure 2.14: Net energy release rate during (a) slow reaction and (b) ignition

radicals. Figure 2.15 presents the results obtained for both the slow reaction and the ignition cases for H and OH. The dominant reaction responsible for the consumption of the H atoms during the slow reaction process is: H + O_2 (+M) $\Longleftrightarrow$ HO_2 (+M), forming less reactive HO_2 radicals. Conversely, during the ignition process, H atoms are primarily consumed through the H + O_2 $\Longleftrightarrow$ OH + O reaction, producing OH radicals. In the slow reaction case, OH radicals are produced by OH elimination reactions and are mainly consumed by the following reactions:

1. CH_2O + OH $\Longleftrightarrow$ HCO + H_2O
2. H_2O_2 + CO + OH $\Longleftrightarrow$ HOCHO + HO_2
3. CH_3HCO + OH $\Longleftrightarrow$ CH_3CO + H_2O
4. C_6H_{14} + OH $\Longleftrightarrow$ cC_6H_{13} + H_2O.

where cC_6H_{13} corresponds the to 3-hexyl radical. The analysis shows that no branching process occurs.

In the ignition case, OH radicals are rapidly produced by the following branching reactions:

1. H + O_2 $\Longleftrightarrow$ OH + O
2. O + H_2 $\Longleftrightarrow$ OH + H
3. H_2O + O $\Longleftrightarrow$ OH + OH

and are consumed by the following exothermic reactions:

1. H + OH (+M) $\Longleftrightarrow$ H_2O (+M)

2. $H_2 + OH \Longleftrightarrow H_2O + H$

3. $CO + OH \Longleftrightarrow CO_2 + H$

The last two reactions also regenerate H atoms.

The consumption of HO_2 radicals is driven by reactions which produce nonreactive species, mainly H_2O_2. In the fast reaction case, their consumption is driven by the $H + HO_2 \Longleftrightarrow OH + OH$ reaction, which produces the very reactive OH radicals. Finally the O atoms take part in the chain branching process: $H + O_2 \Longleftrightarrow OH + O$ and $O + H_2 \Longleftrightarrow OH + H$, but only during the ignition event and not during the slow reaction.

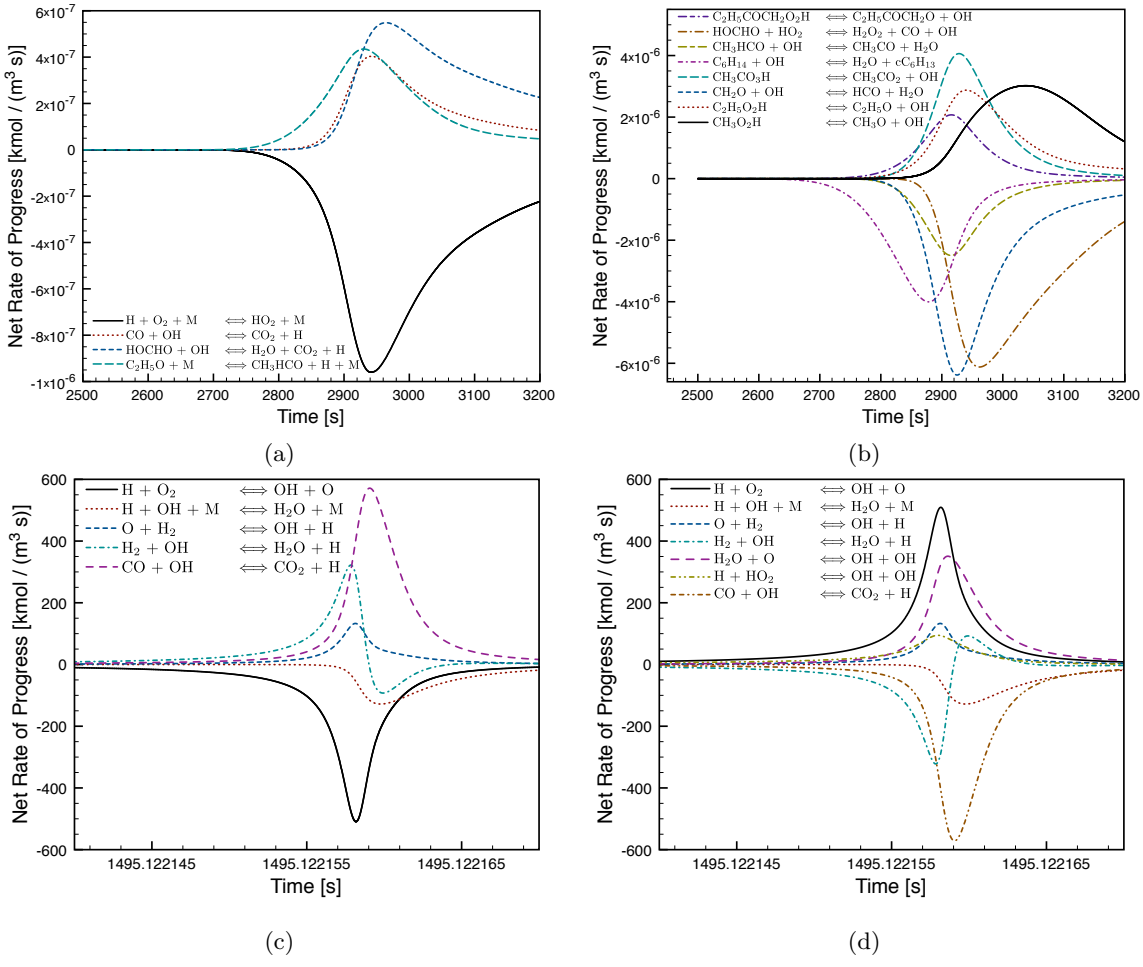

Figure 2.15: Rate of production of H atoms and OH radicals for a $\Phi = 1.2$ n-hexane-air mixture and two different heating rates: (a) and (b), $\alpha = 5$ K/min; (c) and (d), $\alpha = 10$ K/min

2.3.1.5 Reaction Pathway Diagrams

A 10% threshold is used for the element flux pathway diagrams in order to underline the most important pathways for both cases. The carbon element pathways for the two phases in the oxidation process are summarized in Figures 2.16 and 2.17. The first phase corresponds to the period where the temperature increases from 500 to 540 K. In the slow reaction case, this period extends from 2350 to 2850 s; for the fast reaction case, it extends from 1220 to 1430 s. As shown in Figure 2.16, the main path for *n*-hexane consumption in both cases is the following:

1. H abstraction by OH from the third carbon atom (C3),
2. O_2 addition on carbon C3,
3. intramolecular H abstraction by O_2 from the fifth carbon atom (C5),
4. second O_2 addition on carbon C5,
5. OH elimination-intramolecular H abstraction by O_2 on carbon C3-cetone formation on carbon C3.

During the slow reaction, a significant amount of the 5-hydroperoxy-hexan-3-one is decomposed into OH, CH_3HCO, and $C_2H_5COCH_2$. The last species is further converted through a series of reactions ultimately leading to CH_2O and C_2H_5O. During the first phase, these reaction rates are almost an order of magnitude higher in the slow reaction case as compared to the ignition case. This is explained by the significantly longer time the mixture spends under these conditions, allowing for an increase in OH concentration, and thus increasing the initiation rate.

During the second phase, additional pathways appear to be important. These are presented in Figure 2.17. For the slow reaction case, this phase extends from 2870 and 3100 s with an increase of temperature of 20 K to reach 560 K. This phase is mainly characterized by successive:

1. CO or CO_2 elimination
2. O_2 addition
3. H addition
4. OH elimination

The overall reaction rate remains the same throughout the entire process ($\sim 10^{-5}$ kmol m^{-3} s^{-1}) and, at 3100 s, 95% of the initial *n*-hexane content is consumed. For the fast reaction case, the second

phase extends from 1430 to 1495 s, at which point ignition occurs, with an increase of temperature until 790 K and reaction rates of the order of 100 times higher than the reaction rates of the slow reaction case in this phase. In this phase, C-C bond rupture is favored over O_2 addition. This process rapidly forms CO which then reacts with OH radicals to form CO_2 and H atoms. This fast production of H atoms, further sustained by the temperature increase, induces an increase in the overall reaction rate through the chain branching reaction H + O_2 $\Longleftrightarrow$ OH + O, and drives the ignition of the mixture. A large amount of O_2 is consumed through addition reactions during the slow reaction. During the fast reaction case, O_2 is still available in the gas phase for the branching process.

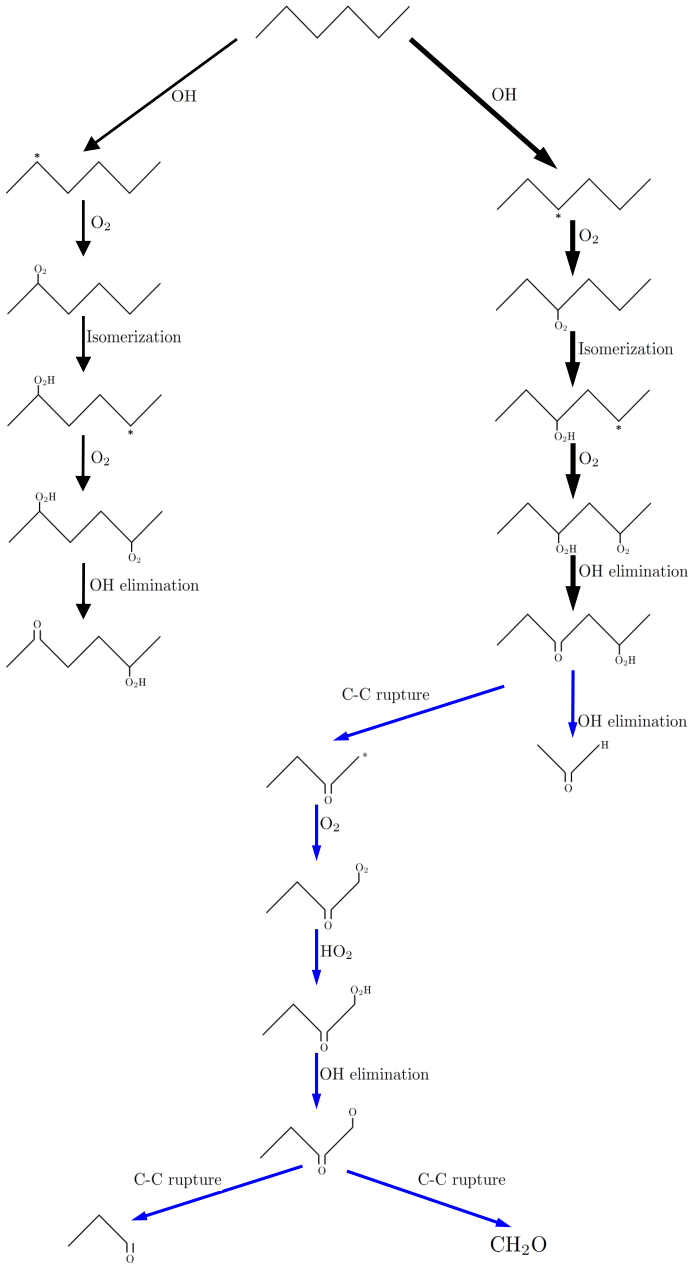

Figure 2.16: Carbon reaction pathways during the first phase of a n-hexane-air mixture oxidation for two heating rates. Conditions: $\Phi = 1.2$; $\alpha = 5$ and 10 K/min. Black arrows: common pathways. Blue arrows: additional pathways observed during the slow reaction. The first phase extends from 2350 to 2850 s for the slow reaction and from 1220 to 1430 s for the fast reaction.

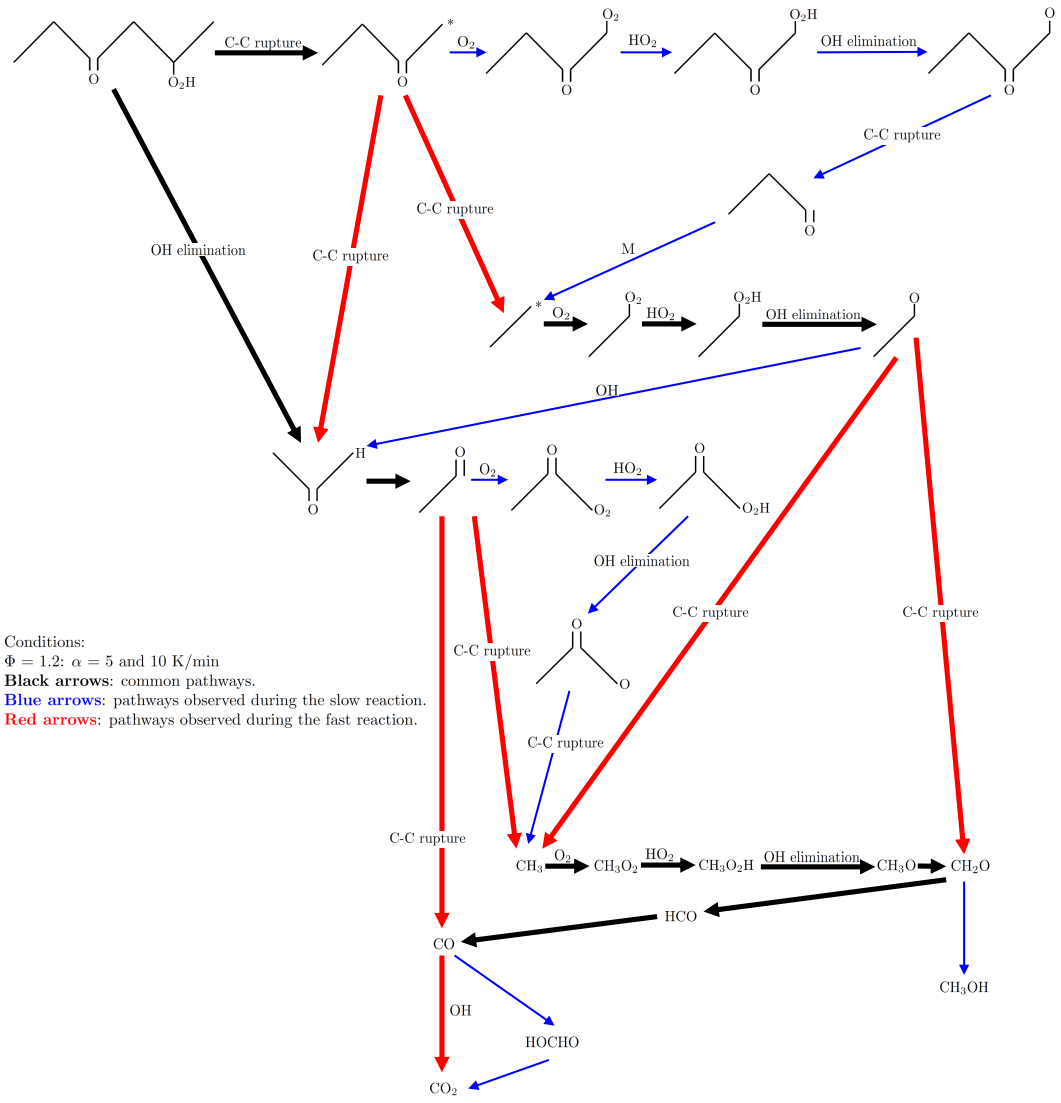

Figure 2.17: Carbon reaction pathways during the second phase of a *n*-hexane-air mixture oxidation for two heating rates. The second phase extends from 2850 to 3100 s for the slow reaction and from from 1430 to 1495 s for the fast reaction.

2.3.1.6 Explosion Limits

Figure 2.18 shows the simulated thermodynamic state trajectories, for the case with $\phi = 1.2$, along with the experimental explosion limits obtained for a 2.7% n-hexane in air by Kane et al. (1937). Figure 2.18 (a) illustrates the temporal evolution whereas Figure 2.18 (b) emphasizes the n-hexane concentration evolution. As shown in Figure 2.18 (a), in the slow reaction case the mixture spends a proportionally long time, several hundred seconds, at a temperature slightly below the auto-ignition temperature 498 K. Due to the extended period the mixture spends at a temperature close to the auto-ignition temperature, more than 50% of reactants are consumed before entering the explosion region. This is shown in Figure 2.18 (b). Both figures together show the importance of considering the evolution, in time and reaction progress, of a particular mixture rather than a simplified threshold point of view.

Analysis of the chemical composition during the slow reaction case shows that mixtures changes significantly from the original $\phi = 1.2$ (2.6%) n-hexane air mixtures into a mix of other hydrocarbons, mainly oxygenated hydrocarbons. The ignition behavior of this mixture is no longer characterized by the explosion limit of the 2.7% n-hexane air mixtures and no ignition is observed as the mixtures enters this ignition region. A slight acceleration of the reaction rate is observed just at the entrance of the explosion region. However, the energy release rate remains too low for ignition to occur and is balanced by the heat-losses at the wall.

Conversely, the fast reaction case progresses much more rapidly, and the mixture quickly enters into the explosion region. In the fast reaction case, although a significant fraction of the reactants, around 10%, is consumed before the mixture enters the explosion region, the composition is not modified enough to avoid explosion and the reactants consumption occurs according to a fast reaction driven by chain branching reactions.

Given the configuration of the experiment, the system has an intrinsic thermochemical feedback loop. By that, we mean the dynamics of the system are controlled by the coupling of the thermodynamic state and the chemical kinetics. Depending on the heating rate, diverging chemical paths occur and in turn influence the evolution of the thermodynamic state.

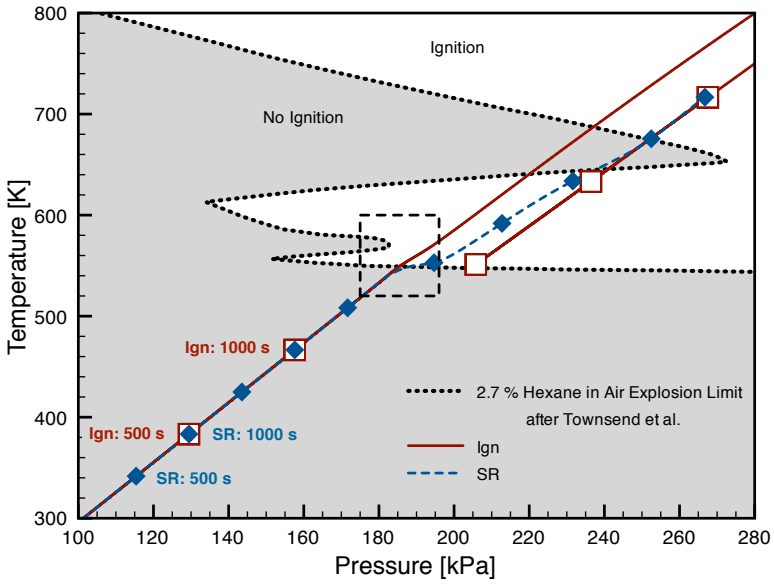

(a)

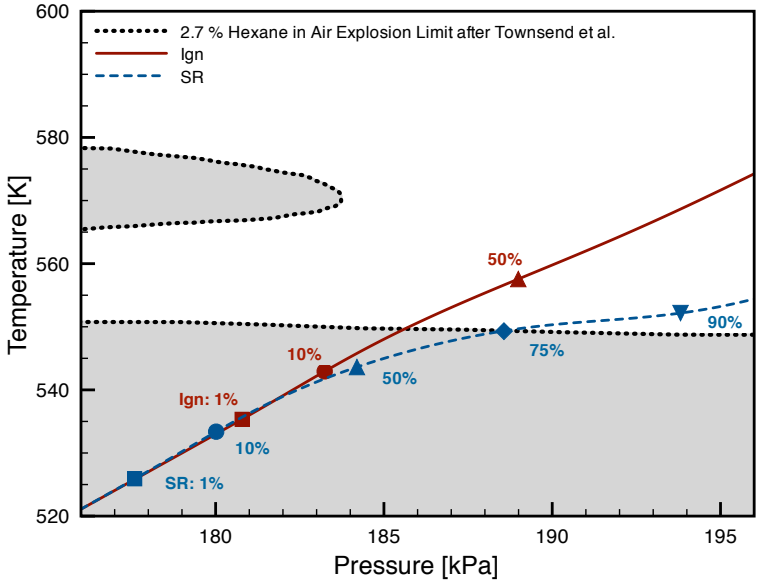

(b)

Figure 2.18: Thermodynamic state trajectories along with the explosion limits (Kane et al., 1937) for a n-hexane-air mixture with different heating rates. Conditions: $\phi = 1.2$; $\alpha = 5$ and 10 K/min; (a): temporal evolution (500 s elapsed time between points). (b): n-hexane percentage consumed in the boxed region of (a)

2.3.1.7 Parametric Study in α, ϕ, and P_0

Through computational simulation of the heated vessel, it is possible to perform a more complete investigation of the behavior as a function of equivalence ratio, initial pressure, and heating rate. The goal is to study the boundary and transformation between a slow reaction and ignition. The simulation is run holding two of the parameters constant and changing the third variable in small increments, with results given in Figures 2.19–2.21. The overpressure created by the reaction is the indicator of ignition and is calculated based on the pressure change relative to the pressure at the time of ignition. Each simulation is run for 3500 seconds, which is sufficient to heat mixtures with heating rates above 5 K/min to temperature higher than 550 K.

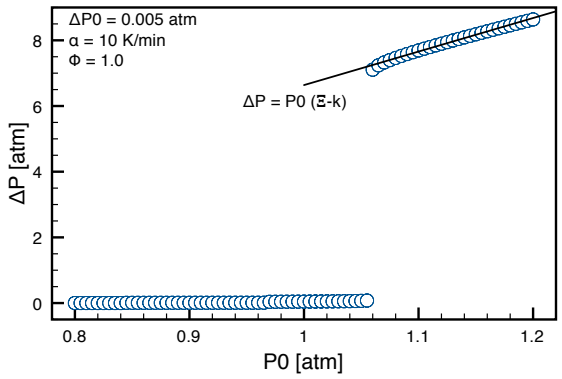

Figure 2.19: Peak overpressure as a function of initial pressure for a stoichiometric mixture of *n*-hexane in air heated at 10 K/min

The first parameter investigated is the pressure, which was shown experimentally to change the behavior from slow reaction to ignition as it is increased (see, for example, shots 4 and 7 in Appendix I). The overpressure is approximately zero until it reaches a critical value and then sharply transitions to large values consistent with an equilibrium calculation for an adiabatic reactor.

For an adiabatic constant volume process at a fixed composition, the ratio of the pressure jump to the initial pressure is basically constant.

$$\frac{\Delta P}{P_0} \cong \text{constant} \tag{2.7}$$

Equivalently, the ratio between the peak pressure, P_p, and pressure at the time of ignition, P_i, is very insensitive to the initial pressure P_0.

$$\Xi = \frac{P_p}{P_0} \tag{2.8}$$

In these simulations, the mixture is heated from room temperature until reaction occurs. The overpressure is the peak pressure minus the pressure at the time of ignition. In the case of slow reactions the peak pressure is the maximum overpressure beyond that of the prescribed ramp.

$$\Delta P = P_p - P_i \tag{2.9}$$

And the pressure just before ignition is also very insensitive to the initial pressure, because the ignition temperature, T_i, is basically constant and the change in the number of moles before ignition can be neglected for this argument. Using the ideal gas assumption, P_i, is given by

$$P_i = P_0 \frac{T_i}{T_0} = kP_0 \ , \tag{2.10}$$

where T_0 is the initial temperature that is held constant. The increasing over pressure with increasing initial pressure for the ignition cases in Figure 2.19 is thus described by

$$\Delta P = P_p - P_i = P_p - kP_0 = P_0 \left(\Xi - k\right) \ . \tag{2.11}$$

In the equation above, for the system we have investigated the constants are $k = 1.83$ and $\Xi = 9.5$ for a stoichiometric mixture.

The next parameter investigated is the heating rate at atmospheric pressure for a stoichiometric mixture ($\phi = 1$). This behavior was the focus of the earlier part of this chapter with experimental results shown in Figures 2.3 and 2.4 for slightly fuel rich mixture ($\phi = 1.2$). The transition point is shifted to a higher transition heating rate than in the fuel-rich case, which is substantiated by the next investigation testing the dependence on equivalence ratio. The overpressure shows a sharp transition from slow reaction cases to ignition cases with increasing α. We see a slight dependence of the overpressure on the heating rate for the ignition cases, which can be attributed to the fact that the heat-loss is reduced with increasing heating rate.

The final parameter that was varied is the equivalence ratio while holding the heating rate and initial pressure constant. The region investigated is between fuel lean to slightly fuel rich mixtures. As with the other two parameters a sharp jump in overpressure is observed with increasing ϕ. The large jump in overpressure for a small change in the equivalence ratio can be attributed to the fact that the mixture energy increases with increasing fuel percentage in this regime and thus the reaction rates, which are highly dependent on the temperature increase drastically. As the equivalence ratio is

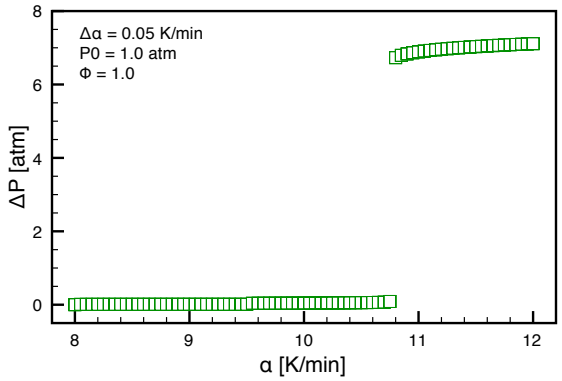

Figure 2.20: Peak overpressure as a function of heating rate for a stoichiometric mixture of n-hexane in air at an initial pressure of one atmosphere

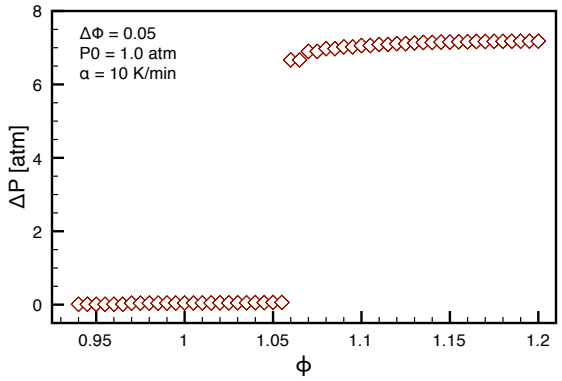

Figure 2.21: Peak overpressure as a function of equivalence ratio for a mixture of n-hexane in air at one atmosphere heated at 10 K/min

increased further, the chemistry changes its pathway away from creating CO_2 and H_2O, which have large heats of formation, to creating CO, breakup of the hydrocarbons and internal H-abstraction resulting in smaller heat release. No experimental data are available that could be compared to simulations run at higher equivalence ratio in an experiment with controlled heating rate.

The final goal of this parametric study is to show the behavior for a range of combinations of all three parameters. Simulations were performed for heating rates between 5 and 15 K/min, in increments of 1 K/min, equivalence ratios from 0.7 to 1.4, in increments of 0.05, and for pressures ranging from 0.5 to 1.2 atmospheres, in increments of 0.1 atm. The results from the atmospheric pressure case in Figure 2.22 show the interdependence between the influence of composition and heating rate. The dashed line indicated the crossover points, i.e., the transition from slow reaction to ignition, extrapolated from the data points, which was performed at each pressure to create Figure 2.24. To check the validity of this extrapolation we performed calculations with a finer grid,

increments of 0.2 K/min for the heating rate and 0.2 for equivalence ratio, at atmospheric pressure only (Figure 2.23). The agreement between the extrapolation from the coarse grid and the fine grid calculations is good, so we have confidence in the final results.

One can note the gaps in the results in Figure 2.23, which are simulations that "crashed", i.e., failed to converge, when calculating the cooling of the system after the temperature spike from the ignition. While there is not question that these points represent ignition cases, they were left in place to stress the difficulty of performing these calculations. For all coarse grid calculations, any missing points were run again with a limited time step size during the cooling phase.

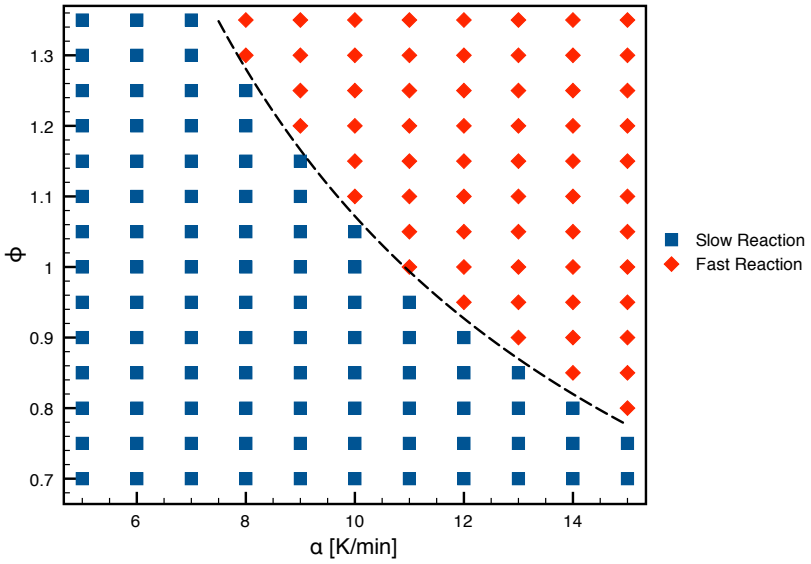

Figure 2.22: Fast reaction and slow reaction cases as a function of equivalence ratio and heating rate at an initial pressure of one atmosphere

The trends shown in the experiments (see Section 2.2.2) for the range we have investigated are confirmed by the calculations presented in Figure 2.24: transition from a slow reaction to ignition occurs by (1) increasing the heating rate, (2) increasing the pressure, and (3) increasing the equivalence ratio (limited to the region shown).

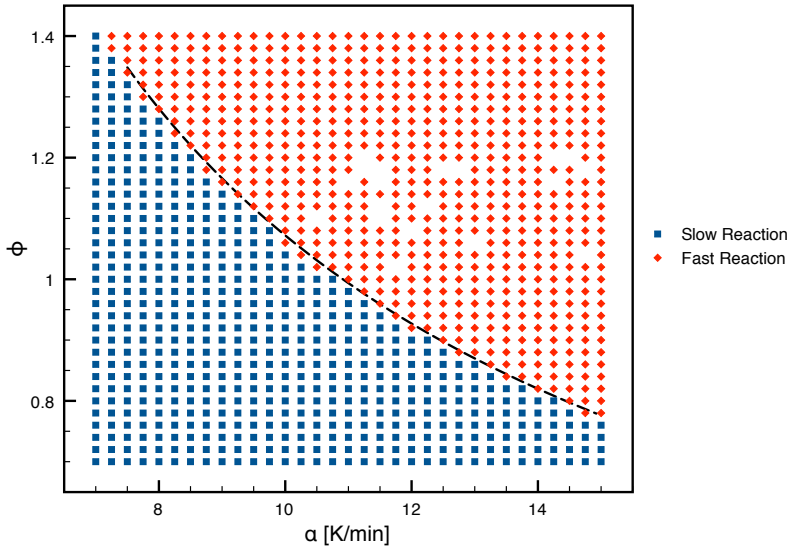

Figure 2.23: Fast reaction and slow reaction cases as a function of equivalence ratio and heating rate at an initial pressure of one atmosphere (fine grid)

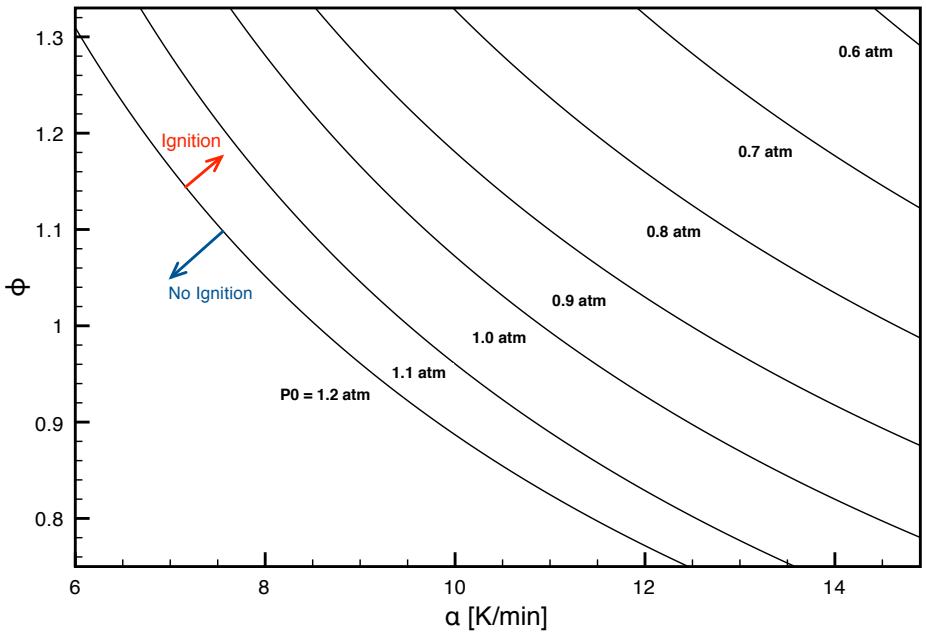

Figure 2.24: Transition limits from slow reaction case to ignition cases as function of the initial pressure, equivalence ration, and heating rate

2.3.2 Modeling with a One-Step Mechanism

The change in behavior from a slow reaction case to an ignition case observed in the experiment and in the detailed chemical analysis is also present when the chemistry is treated with a simple one-step mechanism. However, only the effect of the heating rate is explored here as the inclusion of effect of pressure and chemical composition are very limited in a one-step model and can be accounted for much more readily in the detailed model.

We follow Semenov's theory (Semenov, 1940) for thermal ignition again assuming a uniform mixture with chemically bound energy. The temperature variation with time is computed from the energy conservation equation, using the nomenclature in Table 2.1,

$$V\rho c_v \frac{dT}{dt} = \dot{q}_r + Sh\left(T_w^0 + \alpha\, t - T\right) = \dot{q}_r + \dot{q}_w \ . \tag{2.12}$$

Table 2.1: Nomenclature

Parameter	Units	Description
T	K	gas temperature
V	m^3	volume
ρ	kg m^{-3}	density
c_v	J kg^{-1} K^{-1}	specific heat at constant volume
q_c	J kg^{-1}	stored chemical energy (heat of combustion)
$\dot{\omega}_i$	kg m^{-3} sec^{-1}	net production rate per unit volume
u_i	J kg^{-1}	internal energy
S	m^2	surface area
h	J sec^{-1} m^{-2} K^{-1}	heat transfer coefficient
T_w^0	K	initial wall temperature
α	K sec^{-1}	wall temperature heating rate
$\dot{q}_r$	J sec^{-1}	energy release rate
$\dot{q}_w$	J sec^{-1}	energy wall loss rate
$\dot{T}_r$	K sec^{-1}	reaction-based temperature change rate
$\dot{T}_w$	K sec^{-1}	wall-based temperature change rate
T_w	K	wall temperature
Q	J m^{-3}	energy density
λ		progress variable
A	sec^{-1}	pre-exponential
E_a	J $kmol^{-1}$	activation energy
$\tilde{R}$	J $kmol^{-1}$ K^{-1}	universal gas constant

We assume that the reaction progresses in one step from reactants (R) to products (P):

$$R \rightarrow P. \tag{2.13}$$

The rate at which this reaction progresses depends to first order on the temperature and to second order on the amount of reactants still present. This dependence is thus governed by an Arrhenius rate law (Glassman, 2008) with depletion,

$$\frac{d\lambda}{dt} = A(1-\lambda)\exp\left(-\frac{E_a}{\tilde{R}T}\right) \tag{2.14}$$

where λ is the reaction progress variable such that $\lambda = 0$ represents reactants and $\lambda = 1$ represents products. The reaction progress can also be interpreted as the relative mass fraction of the deficient reactant; for lean mixtures the deficient reactant is the fuel, and for rich mixtures the deficient reactant is the oxidizer. In the Arrhenius rate, E_a is the activation energy and A is the pre-exponential coefficient.

The heat release rate into the reactor is thereby the total energy contained in the system times the consumption rate

$$\dot{q}_r = \rho V q_c \frac{d\lambda}{dt} = VQ\frac{d\lambda}{dt}\ . \tag{2.15}$$

The chemical energy released per unit mass of reactant, q_c, can be estimated from an equilibrium calculation of a given mixture at constant internal energy and volume.

Table 2.2 shows the parameters chosen for the simulation. The first set is chosen to directly reflect the experimental setup. The heat release and specific heat are calculated using Cantera using the equilibrium calculations for a constant volume explosion (Goodwin, 2003). The specific heat is averaged between the initial and final conditions. The activation energy is estimated from the slope of the ignition delay time at low temperatures in the Arrhenius plot (Figure 2.25) and is consistent with literature values (Burcat et al., 1996). Finally, the pre-exponential is selected empirically so that a transition occurs from a slow reaction case to an ignition case when changing the heating rate from 5 K/min to 10 K/min.

While an upper bound for the pre-exponential can be estimated for an elementary reaction by calculating the collision frequency between molecules (see Appendix D), this estimate does not necessarily hold for a global reaction. Nevertheless, the value found here for the pre-exponential, A, is consistent with values from the literature. Westbrook and Dryer (1984) find $A = 5.7 \times 10^{11}$ s^{-1}, but consider a lower activation energy of $E_a = 30$ kcal/mol.

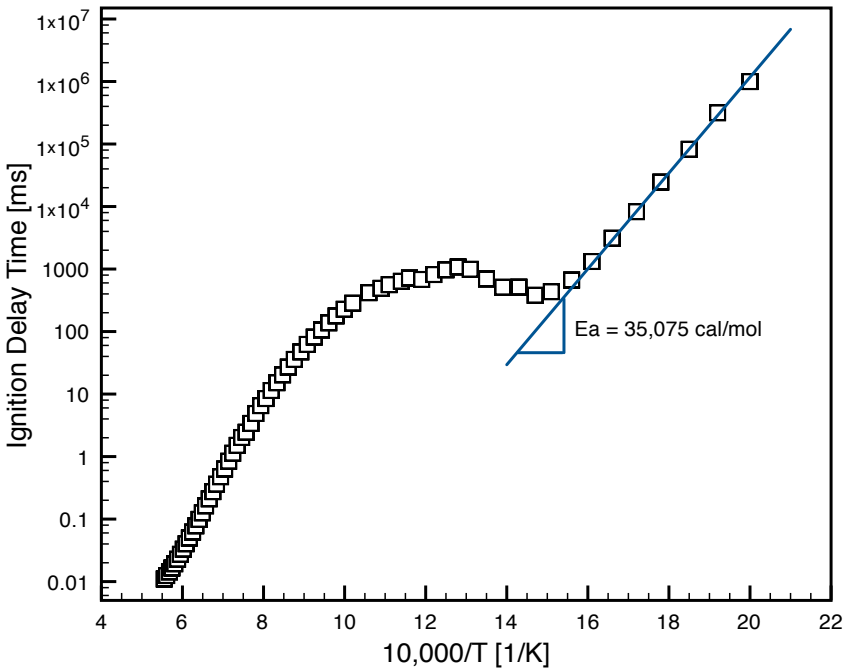

Figure 2.25: Ignition delay time as a function of reciprocal temperature for a stoichiometric hexane-air mixture at atmospheric pressure. The activation energy at low temperatures is estimated by the slope indicated.

Table 2.2: Parameters used in modeling of hexane-air auto-ignition

Parameter		Units	Description
ρ_0	1.24	kg m^{-3}	unburnt gas density
T^0	298	K	initial temperature
T_w^0	298	K	initial wall temperature
V	427	cm^3	gas volume
S	0.05	m^2	surface area of the vessel
q_c	2.3×10^6	J kg^{-1}	stored chemical energy
c_v	930	J kg^{-1} K^{-1}	average specific heat of the gas mixture at constant volume
E_a	35075	cal kmol^{-1}	activation energy
	146754	J kmol^{-1}	activation energy
A	3.3×10^{14}	s^{-1}	pre-exponential

The results from the simulation using the same heating rates as in the experiments and detailed chemistry modeling are given in Figures 2.27 and 2.26. The values used are given in Table 2.2. The slow reaction case shows the gradual progress of the reaction along with the slight increase of the temperature above the ramp rate. The 10 K/min heating rate case shows the sharp jump in consumption after has reached approximately 60% products, which is accompanied with the large increase in temperature above the prescribed ramp rate. These results are in good agreement with those using the detailed chemical mechanism shown in Figure 2.11.

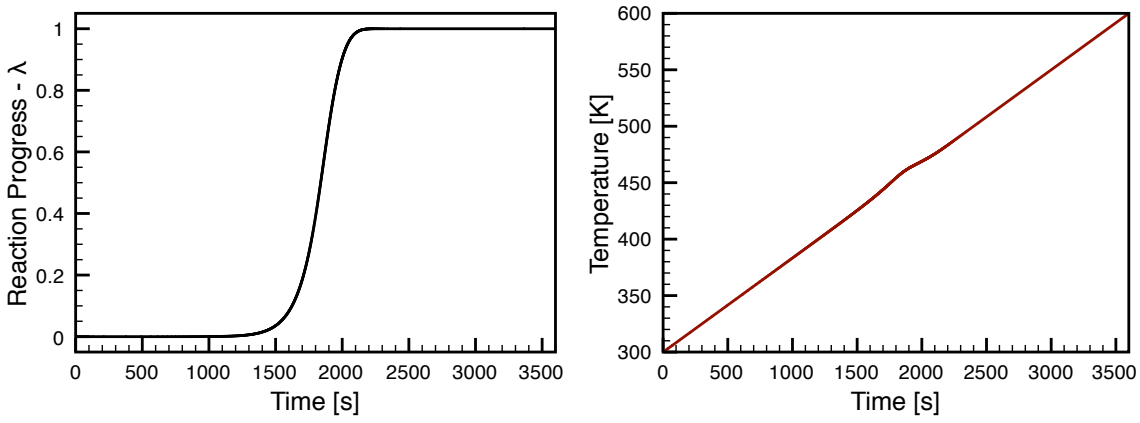

(a) (b)

Figure 2.26: Simulated slow reaction for a heating rate of $\alpha = 5$ K/min using one-step chemistry; (a) reaction progress, (b) temperature

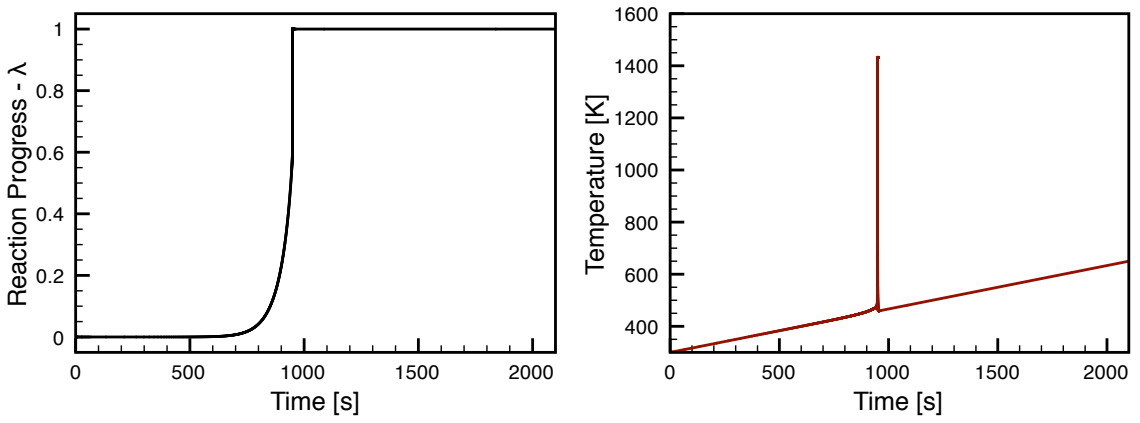

(a) (b)

Figure 2.27: Simulated ignition for a heating rate of $\alpha = 10$ K/min using one-step chemistry; (a) reaction progress, (b) temperature

This analysis using the one-step model for the reaction progress demonstrates that slow reactions are not dependent on the the specific chemical processes that occur, which were explored earlier,

but rather the combination of the thermodynamic state and the extend to which the reaction has progressed.

2.4 Theoretical Considerations

Thermal ignition has been analyzed by many authors like Semenov (1940) and Frank-Kamenetskii (1969) and is described in many text books such as "Combustion" by Glassman (2008). However, these studies did not include the effect of ramp heating or include the transition between slow and fast explosions. Our objective is to extend previous work to include the effect of heating rate and examine the role of the heating rate in the transition from slow to ignition events. The energy equation, given in Equation 2.16, and the one-step reaction progress equation, given in Equation 2.17, form the basic set for our theoretical analysis of the ramp-heated vessel.

$$\frac{dT}{dt} = \frac{QA}{\rho c_v}(1-\lambda)\exp\left(-\frac{E_a}{\tilde{R}T}\right) + \frac{Sh}{\rho V c_v}\left(T_w^0 + \alpha t - T\right) \tag{2.16}$$

$$\frac{d\lambda}{dt} = A(1-\lambda)\exp\left(-\frac{E_a}{\tilde{R}T}\right) \tag{2.17}$$

The nomenclature is the same as for the one-step model given in Table 2.1. Equation 2.16 can be rewritten to reveal several time scales that are in competition,

$$\frac{dT}{dt} = \frac{T_{ref}}{t_r}(1-\lambda)\exp\left(-\frac{E_a}{\tilde{R}T}\right) - \frac{1}{t_w}\left(T - T_w^0\right) + \frac{t\,T_{ref}}{t_w\,t_\alpha}\ , \tag{2.18}$$

which are the chemical energy release time,

$$t_r = \frac{\rho c_v T_{ref}}{QA}\ , \tag{2.19}$$

the wall heat transfer time,

$$t_w = \frac{\rho V c_v}{Sh}\ , \tag{2.20}$$

and ramp heating time,

$$t_\alpha = \frac{T_{ref}}{\alpha}\ . \tag{2.21}$$

T_{ref} is a reference temperature, such as the ignition temperature. In the following sections, we will explore the competition between the physical processes represented by these time scales and the effect of reaction consumption.

2.4.1 Ignition With Negligible Consumption

As a first approximation, we can consider a volume of flammable gas where the consumption of fuel can be neglected. While interesting solutions can be found by neglecting consumption, we subsequently have to revisit this assumption in order to address the transition between slow and fast reactions. The set of governing equations in this case reduces to the energy equation with $\lambda = 0$,

$$\frac{dT}{dt} = \frac{QA}{\rho c_v} \exp\left(-\frac{E_a}{\tilde{R}T}\right) + \frac{Sh}{\rho V c_v}\left(T_w^0 + \alpha t - T\right) \ . \tag{2.22}$$

We can investigate the extensions of two classical theories of ignition, the adiabatic explosion and the explosion with heat-loss and examine how including a wall heating rate changes the results.

2.4.1.1 Dominant Chemical Energy Release

In the limit when the heat release time scale, t_r, is much shorter the heat transfer time scale, t_w, the first term Equation 2.18 dominates and the energy equation reduces to the following form:

$$\frac{dT}{dt} = \frac{QA}{\rho c_v} \exp\left(-\frac{E_a}{\tilde{R}T}\right) \ . \tag{2.23}$$

This situation is the classical adiabatic thermal explosion, in which a mixture is suddenly increased to a temperature T_0 and after a certain induction time, τ_c, the mixture ignites with a large temperature spike. The induction time is also called the ignition delay time, as it often studied by elevating the temperature of a mixture by, for example, a shock wave, and then measuring the delay between the sudden temperature rise and the ignition event.

The ignition delay time can be found readily by simplifying the analysis one step further and assuming large activation energy as done by Frank-Kamenetskii (1969) (see C.2.2). The temperature is expanded for small perturbations about the initial temperature, $T = T_0 + T'$, resulting in

$$\frac{d\theta}{d\tau} = e^{\theta} \ , \tag{2.24}$$

where

$$\tau = \frac{t}{\tau_c} \ , \tag{2.25}$$

$$\theta = \frac{E_a T'}{\tilde{R}{T_0}^2} \ . \tag{2.26}$$

Equation 2.24 can now be integrated directly.

$$\int_0^{\tau} d\tau' = \int_0^{\theta} e^{-\theta'} d\theta' \tag{2.27}$$

$$\theta = -\ln(1-\tau) \tag{2.28}$$

We can now see see that the temperature will tend to $+\infty$ when $\tau = 1$, which is the induction time $t = \tau_c$. The infinite temperature is clearly nonphysical and a consequence of neglecting reaction consumption.

Two derivations are given Appendix C.2 that build on the one given above and those found in text books (Law, 2006, Glassman, 2008) leading to the final equation for the ignition delay time, τ_c,

$$\tau_c = \frac{\rho c_v}{QA} \frac{T_0^2 \tilde{R}}{E_a} \exp\left(\frac{E_a}{\tilde{R} T_0}\right). \tag{2.29}$$

The equation shows that the ignition delay time has a very strong temperature dependence (Law, 2006) and the results of an ignition delay time study are usually plotted as shown earlier in Figure 2.25. It is an important design parameter for many combustion applications as it describes the explosion time for a homogeneous adiabatic reactor, but the ignition delay time is not an appropriate quantity to estimate the ignition time in low temperature safety situations. In these situations, such as ignition time of fuel spilled in an engine compartment or leaked to a compartment adjacent to a fuel tank that is kept at relatively low temperatures, the loss terms and reaction consumption cannot be neglected.

2.4.1.2 Effect of Ramp Rate on Induction Time

Now that we have established the ignition delay time for an adiabatic system, we now consider the effect of heating the walls and investigate the effect of the heating rate, α, on the ignition delay time.

The temperature evolution of a system with a wall temperature ramp and heat transfer in given in Appendix C.2.3. At late times, the temperature ramp inside follows the prescribed ramp rate outside

$$\frac{dT}{dt} = \alpha \,. \tag{2.30}$$

Neglecting reactant consumption, the chemical energy release can now be considered as an ad-

dition to the temperature ramp:

$$\frac{dT}{dt} = \frac{QA}{\rho c_v} \exp\left(-\frac{E_a}{\tilde{R}T}\right) + \alpha \ . \tag{2.31}$$

Since the equation is separable, direct integration is possible,

$$\int_0^t dt' = \int_{T_0}^{T} \frac{1}{k \exp\left(-\frac{E_a}{\tilde{R}T'}\right) + \alpha} dT' \ , \tag{2.32}$$

where $k = QA/\rho c_v$. However, we must make an approximation to find an analytic solution.

$$\int_0^t dt' = \int_{T_0}^{T} \frac{1}{k} \exp\left(\frac{E_a}{\tilde{R}T'}\right) \left(1 - \frac{\alpha}{k \exp\left(-\frac{E_a}{\tilde{R}T'}\right)} + \left(\frac{\alpha}{k \exp\left(-\frac{E_a}{\tilde{R}T'}\right)}\right)^2 - \cdots\right) dT' \tag{2.33}$$

This series converges only for

$$\frac{\alpha}{k \exp\left(-\frac{E_a}{\tilde{R}T'}\right)} < 1 \tag{2.34}$$

which is a reasonable assumption, holding true for $T' > 410$ K given the values in Table 2.2 at a heating rate of 10 K/min. Thus it is possible to determine, by inspecting the integrals, that the time until ignition, t_{ign} is shorter when the external wall temperature is ramped up.

$$t_{ign} = \int_{T_0}^{T} \frac{1}{k} \exp\left(\frac{E_a}{\tilde{R}T'}\right) \left(1 - \frac{\alpha}{k \exp\left(-\frac{E_a}{\tilde{R}T'}\right)}\right) \tag{2.35}$$

The detailed behavior, of course depends on the different parameters, such as the activation temperature, $T_a = E_a/\tilde{R}$, or k. Varying the initial temperature, T_0, and numerically integrating both Equation 2.23 and Equation 2.32 gives the ratio, r, between the delay time with and without wall heating in Figure 2.28. The results show how the addition of a wall temperature ramp decreases the ignition delay time and its influence is increased the longer the initial ignition delay time is.

$$r = \int_{T_0}^{T} \frac{1}{k \exp\left(-\frac{E_a}{\tilde{R}T'}\right)} dT' \Bigg/ \int_{T_0}^{T} \frac{1}{k \exp\left(-\frac{E_a}{\tilde{R}T'}\right) + \alpha} dT' \tag{2.36}$$

Equation 2.31 does not describe the system accurately because the ramp heating rate is directly coupled to the heat transfer (see Equation 2.22). The derivation described here is therefore more a thought experiment of what would happen to the induction time if the mixture temperature were to increase at a given rate. The main observation from Figure 2.28 is that ratio of induction times is less

than one, i.e., an added temperature increase will shorten the induction time. For the overall system, this implies that system which ignite will even ignite faster if the temperature is increased from the outside or inside. A possibility for this internal temperature ramp could be nuclear reactions not captured in the chemical energy.

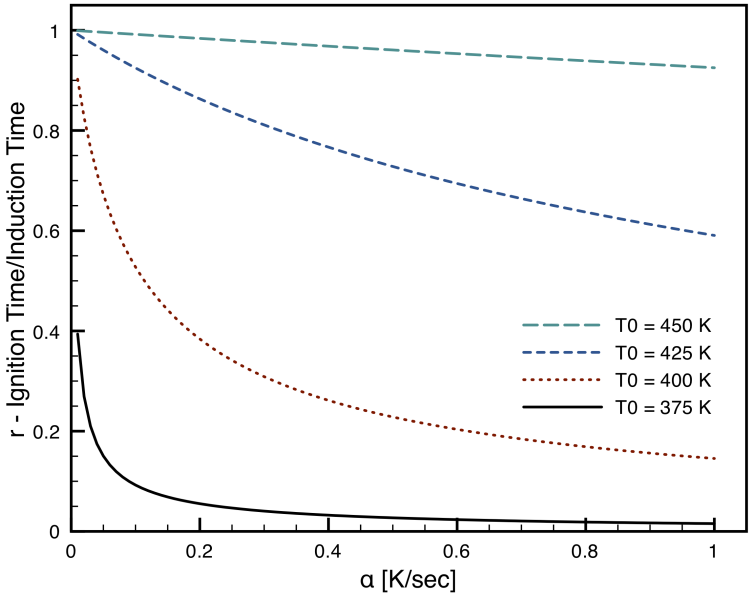

Figure 2.28: Ramp rate reduced induction time

2.4.1.3 Critical Heat Transfer

If we include heat transfer to the wall, but omit the wall temperature ramp ($\alpha = 0$), we can reach solutions which depend on the initial temperature of the mixture. This classical scenario is often called the Semenov problem since he first considered it (Semenov, 1940), and it is discussed in text books (Glassman, 2008, Law, 2006). The energy conservation equation now becomes

$$\frac{dT}{dt} = \frac{QA}{\rho c_v} \exp\left(-\frac{E_a}{\tilde{R}T}\right) - \frac{Sh}{\rho V c_v}\left(T - T_w^0\right) \ , \tag{2.37}$$

which can be reduced to the following form with similar approximations as in the previous section (see Appendix C.2.5 for details)

$$\frac{d\theta}{d\tau} = e^{\theta} - \hat{h}\theta = \dot{T}_r + \dot{T}_w \ . \tag{2.38}$$

The equation shows the direct competition between the energy release rate and the heat-loss rate. This competition can be visualized by plotting the reaction-based temperature change rate, $\dot{T}_r$, and the wall-based temperature change rate, $\dot{T}_w$, as a function temperature, θ, as shown in Figure 2.29. If

the heat transfer coefficient is below the critical value, $\hat{h} = e$, the chemical energy release rate exceeds the heat-loss rate for all temperature values. At the critical heat transfer value, $\dot{T}_w = -e \cdot \theta$, we can reach an unstable equilibrium point, point "a", where the heat-loss rate equals the release rate, but any increase in temperature leads to ignition. For higher values of the heat transfer coefficient, a stable equilibrium point, point "b", and a unstable equilibrium point, point "c", can be reached depending on the initial temperature. At point "b", an increase in temperature lead the heat-loss to exceed the chemical heat release and system will return back to "b". At point "c" increasing the temperature creates a runaway reaction, where the heat-loss can never catch up with the heat release again.

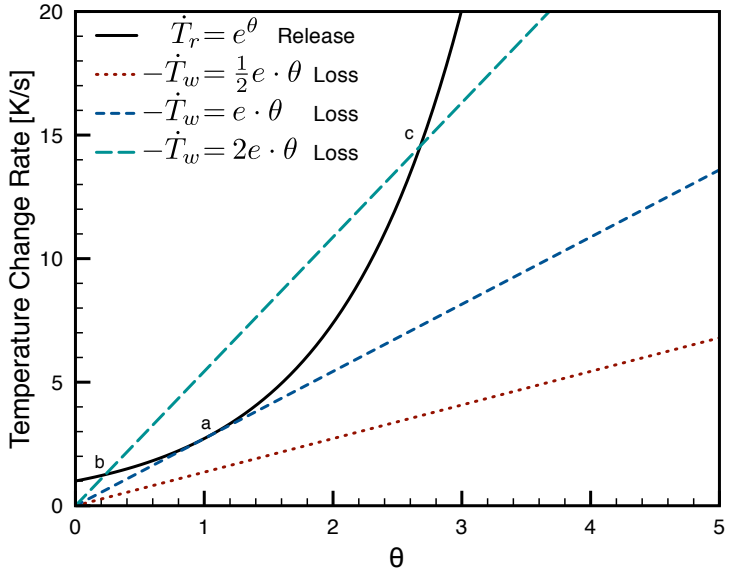

Figure 2.29: Absolute values of heat release and heat-loss components of the energy equation (after Law, 2006)

2.4.1.4 Critical Time For Wall Temperature Ramp

Now, we consider the competition between the chemical energy release and heat-loss with an increasing wall temperature. This means we are considering the full energy equation, but are still neglecting species consumption

$$\frac{dT}{dt} = \frac{QA}{\rho c_v} \exp\left(-\frac{E_a}{\tilde{R}T}\right) + \frac{Sh}{\rho V c_v} \left(T_0 + \alpha t - T\right) \ . \tag{2.39}$$

Here, the initial temperature is the wall temperature since we assume to start far away from the activation temperature, $T_a = E_a/\tilde{R}$, implying that the initial consumption is small. The evolution

of the temperature is considered to be a small deviation, T', from the initial temperature, T_0,

$$T = T_0 + T' \ . \tag{2.40}$$

The energy equation can then be simplified using the large activation energy assumption (see C.2.2),

$$\frac{dT'}{dt} = \frac{1}{\tau_c}\frac{\tilde{R}{T_0}^2}{E_a}\exp\left(\frac{E_a T'}{\tilde{R}{T_0}^2}\right) + \frac{1}{t_w}\left(\alpha t - T'\right) \ , \tag{2.41}$$

using the previously defined the wall heat transfer time

$$t_w = \frac{\rho V c_v}{Sh} \ , \tag{2.42}$$

and the ignition delay time

$$\tau_c = \frac{\rho c_v}{QA}\frac{{T_0}^2\tilde{R}}{E_a}\exp\left(\frac{E_a}{\tilde{R}T_0}\right) . \tag{2.43}$$

The temperature, time and other parameters can be nondimensionalized as follows:

$$\tau = \frac{t}{\tau_c} \tag{2.44}$$

$$\theta = \frac{E_a T'}{\tilde{R}{T_0}^2} \tag{2.45}$$

$$\hat{h} = \frac{\tau_c}{t_w} \tag{2.46}$$

$$\tilde{\alpha} = \frac{\alpha T_a \tau_c}{{T_0}^2} \ . \tag{2.47}$$

The nondimensional energy equation now is

$$\frac{d\theta}{d\tau} = e^{\theta} + \hat{h}\left(\tilde{\alpha}\tau - \theta\right) = \dot{\Theta}_r + \dot{\Theta}_w \ , \tag{2.48}$$

where the nondimensional reaction-based and wall-based temperature change rates are

$$\dot{\Theta}_r = e^{\theta} \tag{2.49}$$

and

$$\dot{\Theta}_w = -\hat{h}\theta + \hat{h}\tilde{\alpha}\tau \ . \tag{2.50}$$

As discussed in the previous section, critical solutions can be observed when the right hand side of the energy equation sums to zero, $d\theta/d\tau = 0$, when the heat transfer coefficient is sufficiently large, $\hat{h} \geq e$. This is observed initially, $\tau = 0$, in a system where the wall temperature is undergoing a ramp heating (see Figure 2.30).

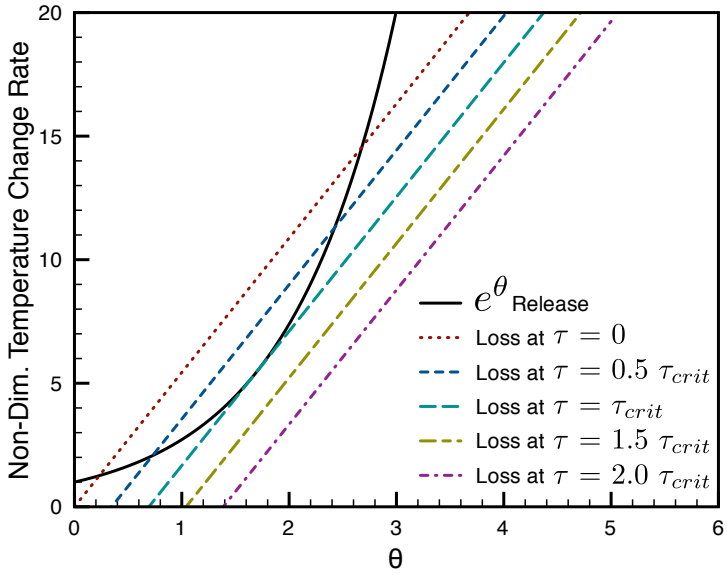

Figure 2.30: Heat release and heat-loss with a wall temperature ramp ($\hat{h} = 2e$)

In system with wall temperature ramp, however, the heat release will eventually always exceed the heat-loss. This point is characterized by not only having the right hand side of the energy equation summing to zero $d\theta/d\tau = 0$,

$$\dot{\Theta}_r = -\dot{\Theta}_w \Longleftrightarrow e^\theta = \hat{h}\theta - \hat{h}\tilde{\alpha}\tau \tag{2.51}$$

and also the he heat release term, $\dot{\Theta}_r$, and heat-loss term, $\dot{\Theta}_w$, being tangent as shown in Figure 2.30 which can be represented as

$$\frac{d\dot{\Theta}_r}{d\theta} = -\frac{d\dot{\Theta}_w}{d\theta} \Longleftrightarrow e^\theta = \hat{h} \tag{2.52}$$

Note that the temperature ramp rate, $\tilde{\alpha}$, is not a function of the temperature. Solving Equation 2.52 for θ and substituting back Eqution 2.51 allows us to solve for the critical time τ_{crit}

$$\hat{h} - \hat{h}\ln(\hat{h}) + \hat{h}\tilde{\alpha}\tau_{crit} = 0 \tag{2.53}$$

$$\tau_{crit} = \frac{\ln\hat{h} - 1}{\tilde{\alpha}}\ . \tag{2.54}$$

This is only of interest for values of $\hat{h} \geq e$, smaller values of $\hat{h}$ yield solutions that always explode faster than τ_{crit}.

Figure 2.30 gives a graphical representation of how the wall heat-loss term, $\dot{\Theta}_w$, evolves in time when a heating ramp is applied. For time less than the critical time, τ_{crit}, the behavior of the system depends on the temperature of the system, i.e., at low temperatures the heat-loss term is greater than the heat release and at large temperature the heat release is always greater than the heat-loss. However, at later times, τ_{crit} and above, the heat release will always exceed the heat-loss. This means that a system that is heated externally will always undergo ignition, as long as consumption can be neglected.

2.4.2 Ignition With Consumption

Treating thermal ignition without consumption is insufficient to explain slow reaction behavior. In this final section of the theoretical treatment consumption is included in the analysis; first without any heat-loss and then considering the full set of equations assuming a one-step model for the chemical reaction. An example of including reaction consumption in a one-step model can be found in Radulescu and Maxwell (2010).

2.4.2.1 Induction Time With Consumption

As a first step we consider how the consumption of reactants changes the induction time, or ignition delay time, explored earlier. Consumption can be reinstated and in the adiabatic case where there is no heat transfer to the wall, the chemical energy is completely converted to thermal energy. This allows us to eliminate the consumption equation. A solution of this problem is discussed in Adler and Enig (1964). The set of equations governing this scenario are the temperature equation from the energy equation

$$\frac{dT}{dt} = \frac{QA}{\rho c_v}\left(1-\lambda\right)\exp\left(-\frac{E_a}{\tilde{R}T}\right) \tag{2.55}$$

and one-step reaction progress equation

$$\frac{d\lambda}{dt} = A\left(1-\lambda\right)\exp\left(-\frac{E_a}{\tilde{R}T}\right) \ , \tag{2.56}$$

where $\lambda = 0$ represents only reactants and $\lambda = 1$ only products. The coupled equations can be simplified to

$$\rho c_v \frac{dT}{dt} = Q\frac{d\lambda}{dt} \ . \tag{2.57}$$

Multiplying through by dt and assuming constant specific heat we can integrate the equation from the initial condition $T = T_0$, $\lambda = 0$,

$$\int_{T_0}^{T} \rho c_v dT^\star = \int_0^\lambda Q d\lambda^\star \ . \tag{2.58}$$

For adiabatic, constant-volume conditions the relationship between chemical and thermal energy can be obtained from the conservation of energy:

$$\rho c_v (T - T_0) = \lambda Q \ . \tag{2.59}$$

The final temperature can be calculated at the time when all fuel is consumed ($\lambda = 1$)

$$T_f = T_0 + \frac{Q}{\rho c_v} \ . \tag{2.60}$$

At any time during the explosion, the progress of the reaction, λ, can then be expressed solely in terms of the fractional temperature rise

$$\lambda (T_f - T_0) = (T - T_0) \ , \tag{2.61}$$

and the energy equation expressed in terms of temperature alone becomes independent of the progress variable

$$\frac{dT}{dt} = \frac{QA}{\rho c_v} \left(\frac{T_f - T}{T_f - T_0} \right) \exp \left(- \frac{E_a}{\tilde{R} T} \right) \ . \tag{2.62}$$

This equation can be integrated for as shown by Hermance (1975) and Parang and Jischke (1975):

$$\int_0^t \frac{QA}{\rho c_v (T_f - T_0)} dt^* = \int_{T_0}^{T} \frac{e^{\frac{E_a}{\tilde{R} T^*}}}{T_f - T^*} dT^* \ . \tag{2.63}$$

The final answer can be expressed in terms of the exponential integral, $Ei(x)$, which is defined as

$$Ei(x) = - \int_x^\infty \frac{e^{-t} dt}{t} \ . \tag{2.64}$$

The solution to Equation 2.63 can be written as

$$t(T) = \frac{\rho c_v (T_f - T_0)}{QA} \times \left[Ei \left(\frac{T_a}{T} \right) - Ei \left(\frac{T_a}{T_0} \right) + e^{\frac{T_a}{T_f}} \left[Ei \left(\frac{T_a}{T_0} - \frac{T_a}{T_f} \right) - Ei \left(\frac{T_a}{T} - \frac{T_a}{T_f} \right) \right] \right] \ . \tag{2.65}$$

where $T_a = E_a/\tilde{R}$ and the solution is only valid for large values of T_a/T_f. To find the induction time a the upper limit should be chosen at $T_f - \epsilon$ as it will take an infinite amount of time to reach T_f yielding a non-physical solution.

As Equation 2.65 shows, the inclusion of consumption results in an analytical solution that is substantially more complex than when consumption is neglected. Further discussion of the solution with consumption is discussed in Adler and Enig (1964), Hermance (1975), and Parang and Jischke (1975).

2.4.2.2 Thermal Ignition with heat-loss, Consumption, and Wall Temperature Ramp

Now, we consider the full set of equations for the ramp heated vessel describing the experimental setup using a one-step model for the chemical reaction progress. Our final goal is to describe how the heating rate changes the behavior from a slow reaction case to an ignition case. Again, the equations describing the system are

$$\frac{dT}{dt} = \frac{Q}{\rho c_v}\frac{d\lambda}{dt} + \frac{Sh}{\rho V c_v}\left(T_w^0 + \alpha t - T\right) \ , \tag{2.66}$$

$$\frac{d\lambda}{dt} = A\,(1-\lambda)\,e^{-\frac{E_a}{\tilde{R}T}} \ . \tag{2.67}$$

The numerical solutions, using the values from Table 2.2, show that the transition from an ignition case to a slow reaction case occurs in a small region of temperature, reaction progress, and time. Figure 2.31 shows an ignition case and a slow reaction case with the transition region indicated in the dashed box.

Taking a closer look at the the indicated transition region, we can observe large changes in temperature, and reaction progress with small changes in time. Computing solutions close to the transition as shown in Figures 2.32 and 2.33, we can see that the transition behavior occur near a specific time, t^*. The transition behavior also occurs near a specific temperature, T^*, and reaction progress, λ^*, most clearly seen Figure 2.34 that shows the numerical results of considering temperature as a function of reaction progress

We can compute an approximate solution of the equations by neglecting chemical reactions, which can serve as a reference case as plotted in Figure 2.34. When setting the heat of reaction to zero, $Q = 0$, the temperature will only increase due to the externally imposed by the wall heating rate (see Appendix C.2.3) and the reaction progress is still governed by the one-step reaction model.

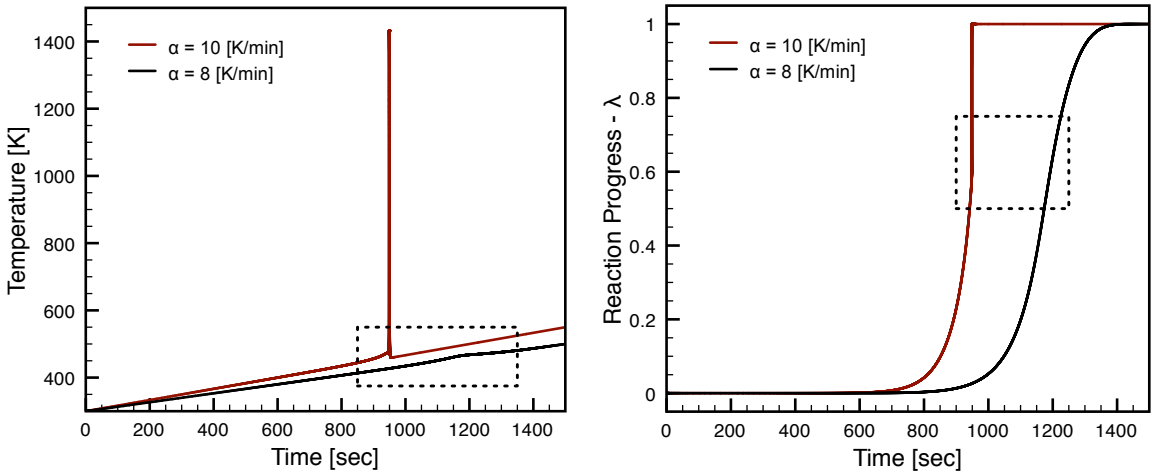

(a) (b)

Figure 2.31: Temperature (a) and reaction progress (b) for a slow reaction case and (8 K/min) and an ignition case (10 K/min). The highlighted region indicates the region where the transition point lies.

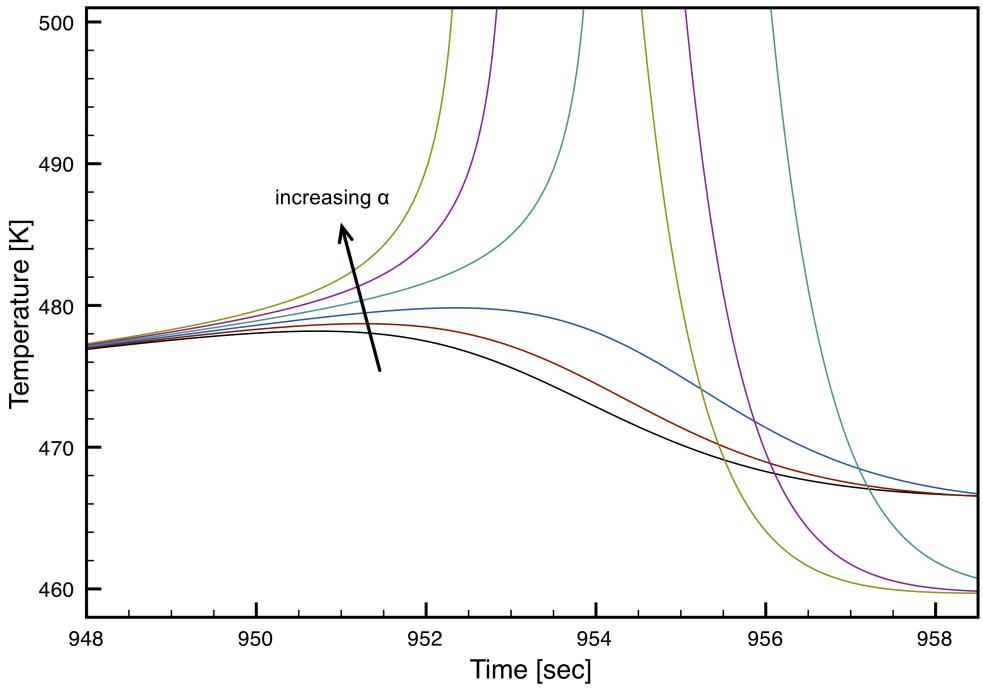

Figure 2.32: Temperature with varying heating rate, α. The curves are spaced equally with increasing heating rates, with a step size of 1.2×10^{-4} K/min (for the lowest curve $\alpha = 9.99546$ K/min).

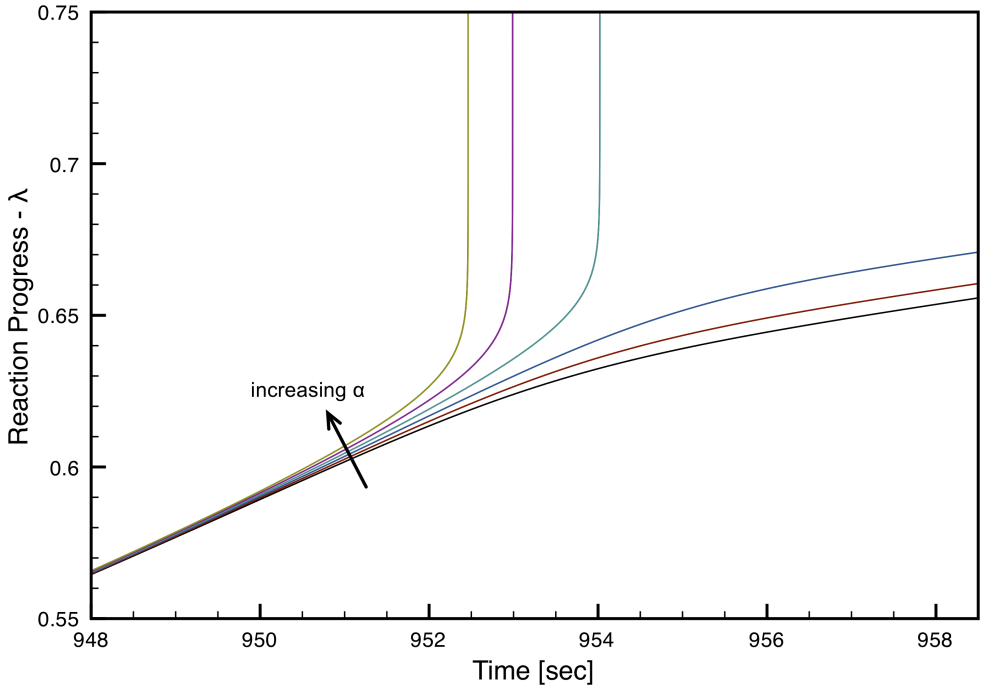

Figure 2.33: Reaction progress with varying heating rate, α. The curves are spaced equally with increasing heating rates, with a step size of 1.2×10^{-4} K/min (for the lowest curve $\alpha = 9.99546$ K/min).

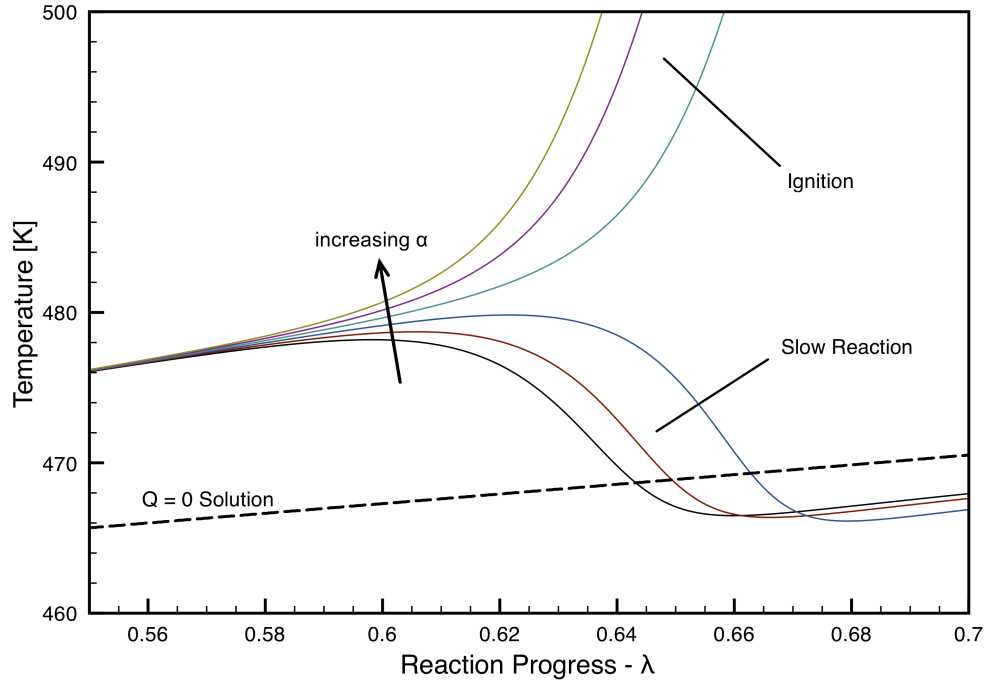

Figure 2.34: Temperature vs. reaction progress with varying heating rate, α. The curves are spaced equally with increasing heating rates, with a step size of 1.2×10^{-4} K/min (for the lowest curve $\alpha = 9.99546$ K/min). The $Q = 0$ solution is computed for the average heating rate value.

$$\frac{dT}{dt} = \alpha \tag{2.68}$$

$$\frac{d\lambda}{dt} = A\left(1-\lambda\right)\exp\left(-\frac{E_a}{\tilde{R}T}\right) \tag{2.69}$$

These two equations can be combined and rearranged to separate the variables,

$$\frac{d\lambda}{1-\lambda} = A\exp\left(-\frac{E_a}{\tilde{R}T}\right)\frac{dt}{dT}dT = A\exp\left(-\frac{E_a}{\tilde{R}T}\right)\frac{1}{\alpha}dT\ . \tag{2.70}$$

This equation can be integrated numerically to yield the approximate solution shown in Figure 2.34

$$\int_0^{\lambda}\frac{d\tilde{\lambda}}{1-\tilde{\lambda}} = \int_{T_0}^{T} A\exp\left(-\frac{E_a}{\tilde{R}\tilde{T}}\right)\frac{1}{\alpha}d\tilde{T}\ . \tag{2.71}$$

The $Q = 0$ solution initially lies below the actual solution because it does not include any heat release from the chemical reaction. Later, the $Q = 0$ solution lies above the full solution for the heat transfer out of the system is sustained as the reaction progresses.

The numerical solutions show that the transition from an ignition case to a slow reaction case occurs over a narrow range of temperature, reaction progress, and time near the transition point (*). The differential equations can be linearized about this transition point (T^*, λ^*, t^*).

$$\lambda = \lambda^* + \lambda' \tag{2.72}$$

$$T = T^* + T' \tag{2.73}$$

$$t = t^* + t' \tag{2.74}$$

We now examine how small changes in the heating rate alter the behavior of the system. To this end it is useful to examine the behavior of the temperature directly as a function of reaction progress, $dT'/d\lambda'$, and then evaluating this dependence that the transition point. Substituting the perturbation into the temperature equation gives:

$$\frac{dT}{dt} = \frac{dT^*}{dt} + \frac{dT'}{dt} = \frac{dT'}{dt} = \frac{Q}{\rho c_v}\frac{d\lambda}{dt} + \frac{Sh}{\rho V c_v}\left(T_w^0 + \alpha\left(t^* + t'\right) - T^* - T'\right)\ . \tag{2.75}$$

The reaction progress equation becomes:

$$\frac{d\lambda}{dt} = \frac{d\lambda^*}{dt} + \frac{d\lambda'}{dt} = \frac{d\lambda'}{dt} = A\left(1-\lambda^*-\lambda'\right)\exp\left(-\frac{E_a}{\tilde{R}\left(T^*+T'\right)}\right) \tag{2.76}$$

Dividing Equation 2.75 by Equation 2.76 gives:

$$\frac{dT'}{d\lambda'} = \frac{Q}{\rho c_v} + \frac{Sh}{A\rho V c_v} \exp\left(\frac{E_a}{\tilde{R}\left(T^* + T'\right)}\right) \frac{T_w^0 + \alpha\left(t^* + t'\right) - T^* - T'}{1 - \lambda^* - \lambda'} \,. \tag{2.77}$$

Now, we can evaluate Equation 2.77 at the the transition point (T^*, λ^*, t^*)

$$\left.\frac{dT'}{d\lambda'}\right|_{T^*,\lambda^*,t^*} = \frac{Q}{\rho c_v} + \frac{Sh}{A\rho V c_v} \exp\left(\frac{E_a}{\tilde{R}T^*}\right) \frac{T_w^0 + \alpha t^* - T^*}{1 - \lambda^*} \tag{2.78}$$

$$\left.\frac{dT'}{d\lambda'}\right|_{T^*,\lambda^*,t^*} = \frac{q_c}{c_v} + \frac{Sh}{A\rho V c_v} \exp\left(\frac{E_a}{\tilde{R}T^*}\right) \frac{T_w^0 + \alpha t^* - T^*}{1 - \lambda^*} \,. \tag{2.79}$$

Equation 2.79 gives the trajectory of the solution from the transition point forward. Positive values indicate ignition, while negative values indicate slow reactions. The switch between the two is an explicit function of the heating rate, α. The high sensitivity to the heating rate can be shown by evaluating the derivative over a range of heating rates using the parameters given in Table 2.2. From the detailed simulations, we can identify roughly where the transition point (T^*, λ^*, t^*) lies, the values for which are given in Figure 2.35. From these values, an approximate value for the transition heating rate, $\alpha^* = 8.1$ K/min, can be computed by setting the left-hand side of Equation 2.79, which is comparable to the critical value found by inspecting the full solutions, $\alpha_c \approx 9.995$ K/min. The switch in sign of the right-hand side of Equation 2.79 is calculated as indicated in Figure 2.35, showing the zero crossing as well as the very large slope indicating the strong dependence on the heating rate.

At the transition point, the sign of $dT'/d\lambda'$ changes based on the value of the heating rate α. While the heating rate is not the only parameter, changing it while keeping all other parameters constant can change the behavior.

The result of the theoretical analysis shows that a switch from slow reaction to ignition can be controlled by a wall temperature ramping, regardless of the chemical mechanism. This is precisely the behavior observed experimentally as well as in the simulations using the detailed chemical mechanism. It underlines the importance of considering the heating rate as one of the parameters controlling the ignition behavior of a mixtures and thus must be taken into account when making assessments regarding ignition safety.

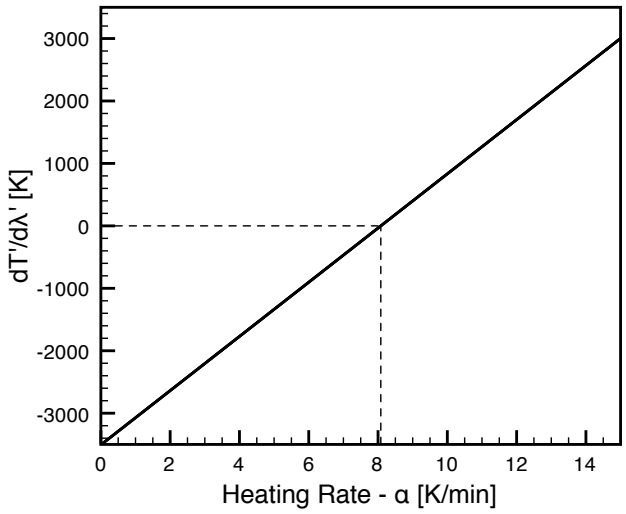

Figure 2.35: Temperature evolution about the transition point as a function of heating rate ($T^* =$ 480 K, $\lambda^* = 0.6$, $t^* = 950$ s)

2.5 Conclusion

In the classical view of auto-ignition, a minimum temperature exists that leads to the ignition of a given fuel under specified conditions. It is known that the auto-ignition temperature depends on many parameters and the present study demonstrates that one of these, the rate at which the mixture is heated, greatly influences how the reaction progresses, and consequently whether the mixture ignites. Further, in contrast to a violent ignition event, we have found slow reaction cases, where it is possible to consume all the fuel without an ignition event at a well-defined temperature.

For instance, increasing the heating rate of the vessel by a factor of 2, from 4.25 to 11 K/min, produces an ignition event with a rapid pressure rise in a mixture that otherwise would have generated a slow reaction with no significant pressure rise. The same transition in behavior is shown for an increase in equivalence ratio from 1 to 1.2. In the range investigated, the minimum heating rate required for fast reactions decreases with increasing equivalence ratios.

The computations demonstrate that a model based on Semenov theory is capable of capturing the qualitative behavior of the explosion event. By adding the heating rate, α, to the classical Semenov model, we are able to reproduce the observed transition from a slow reaction case to an ignition case with increasing heating rate; with the necessity of determining the lumped heat transfer coefficient empirically.

The simulations results are not limited to detailed chemical mechanisms, but also hold when the chemistry is approximated by a one-step model. Through the theoretical treatment, we can clearly

determine that the heating rate switches the mixture evolution from slow reactions to ignitions.

The type of reaction that the mixture undergoes is a complex function of the mixture composition, thermochemical feedback loop, residence time, and heat transfer. Consequently, for sufficiently slow heating rates, it is possible for the fuel to be completely consumed without any rapid pressure transient at temperatures above the classical auto-ignition value. The experimental results also indicate that the transitional heating rate is a function of the initial pressure and composition.

The results presented here show that an assessment of safety should include factors such as the temperature, pressure, mixture composition, and heating rate rather than just a threshold temperature when considering auto-ignition. For instance, the temperatures at which the reactions occur are near the listed auto-ignition temperatures for the slow reaction case, but slightly below for the ignition case. These factors come into play both when designing a standard test procedure to determine fuel properties as well as assessing the safety of a particular engineering design.

The simulations show that the slow reaction and ignition behavior can be modeled correctly, however due to the complex chemical pathways and limited data on fuels like n-hexane at low temperatures it is difficult do predict the temperature at the onset of reaction to an accuracy better than 50 K.